

Manuscript Number: BONE-D-19-00679R1

Title: Reduction of fibrillar strain-rate sensitivity in steroid-induced osteoporosis linked to changes in mineralized fibrillar nanostructure

Article Type: SI: Celebrating John Currey: Regular MS

Keywords: Glucocorticoid induced osteoporosis; Synchrotron X-ray nanomechanical imaging; Nanoscale deformation mechanisms; Multiscale mechanical modelling

Corresponding Author: Dr. Himadri Gupta,

Corresponding Author's Institution: Queen Mary University of London

First Author: Li Xi

Order of Authors: Li Xi; Paolino De Falco; Angelo Karunaratne; Liz Bentley; Chris Esapa; Graham R Davis; Nicholas J Terrill; Roger D Cox; Nicola M Pugno; Rajesh V Thakker; Richard Weinkamer; D N Fang; Himadri Gupta

Abstract: As bone is used in a dynamic mechanical environment, understanding the structural origins of its time-dependent mechanical behaviour - and the alterations in metabolic bone disease - is of interest. However, at the scale of the mineralized fibrillar matrix (nanometre-level), the nature of the strain-rate dependent mechanics is incompletely understood. Here, we investigate the fibrillar- and mineral-deformation behaviour in a murine model of Cushing's syndrome, used to understand steroid induced osteoporosis, using synchrotron small- and wide-angle scattering/diffraction combined with in situ tensile testing at three strain rates ranging from 10^{-4} to 10^{-1} s $^{-1}$. We find that the effective fibril- and mineral-modulus and fibrillar-reorientation show no significant increase with strain-rate in osteoporotic bone, but increase significantly in normal (wild-type) bone. By applying a fibril-lamellar two-level structural model of bone matrix deformation to fit the results, we obtain indications that altered collagen-mineral interactions at the nanoscale - along with altered fibrillar orientation distributions - may be the underlying reason for this altered strain-rate sensitivity. Our results suggest that an altered strain-rate sensitivity of the bone matrix in osteoporosis may be one of the contributing factors to reduced mechanical competence in such metabolic bone disorders, and that increasing this sensitivity may improve biomechanical performance.



Queen Mary, University of London
Mile End Road, London E1 4NS
Telephone: +44(0)20 7882 5555
Fax: +44(0)20 8983 1007

School of Engineering & Materials Science
H. S. Gupta, MSc, PhD
Reader in Bioengineering and Biophysics
Direct Tel: +44(0)20 7882 8867
Email: h.gupta@qmul.ac.uk

13 October, 2019

To the Editorial Board of *Bone*

Manuscript submission: "*Reduction of fibrillar strain-rate sensitivity in steroid-induced osteoporosis linked to changes in mineralized fibrillar nanostructure*" -Revision

Dear Editor,

I am submitting, as corresponding author, our revised manuscript entitled "*Reduction of fibrillar strain-rate sensitivity in steroid-induced osteoporosis linked to changes in mineralized fibrillar nanostructure*" for your consideration for publication in *Bone*.

Our Reviewer Response is in the attached file, with Reviewer and Editor comments in red, our response in blue font, and changed text in blue highlight. In the revised manuscript, changed text is in blue highlight. This paper is submitted for the special issue honouring Prof. John Currey.

Sincerely yours, on behalf of all the authors,

A handwritten signature in blue ink that reads "Himadri S. Gupta".

Dr. Himadri S. Gupta
Reader in Bioengineering and Biophysics
Institute of Bioengineering and School of Engineering and Materials Science
Queen Mary University of London, Mile End Road, London E1 4NS, UK
Email: h.gupta@qmul.ac.uk

Patron: Her Majesty the Queen

Incorporated by Royal Charter as
Queen Mary and Westfield College,
University of London

Editor comment 1:

Highlights consist of a short collection of bullet points that convey the core findings of the article and should be submitted in a separate file in the online submission system. Please use 'Highlights' in the file name and include 3 to 5 bullet points (maximum 85 characters, including spaces, per bullet point). See the following website for more information

Highlights – key findings

- Mineralized fibrils in healthy mouse bone show strain-rate dependent stiffening.
- The fibrillar stiffening is absent in steroid-induced osteoporosis.
- Modelling suggests altered collagen-mineral interactions may explain this change.
- Changed fibrillar stiffening may be relevant to altered mechanics in osteoporosis.

Author response to Reviewer comments:

We thank both Reviewers for their positive comments. e.g.

Reviewer #1: “...*This paper provides interesting information about the dynamic response of bone with and without GIOP at the nano-scale. I find no fault in the execution of the experiments which appear to have been thoughtfully planned and executed. ...*”.

Reviewer #2: “...*This is an interesting article and will make a significant contribution in this special issue of BONE dedicated to J Currey's inspiring life time of work on bone....*”

as well as their insightful comments. Below we list the comments in red and our response in blue. New text additions to the MS are indicated in blue highlight both in the revised MS and in the current document.

Reviewers' comments:

Reviewer #1 (R1):

This paper provides interesting information about the dynamic response of bone with and without GIOP at the nano-scale. I find no fault in the execution of the experiments which appear to have been thoughtfully planned and executed. However, I have a few questions about analysis and interpretation:

R1-1: In the uCT data you clearly see that the endosteal region of the GIOP bone is significantly

more porous than the WT. Could you report the porosity of the bone? This would be useful along with the mean mineral concentration.

AR1-1: Yes, we added the porosity of bone in the revised paper. The porosity was calculated as (area of pores / bone cross section area) * 100%, as analyzed from backscattered electron (BSE) imaging of the cross section of femoral mid-diaphysis of wild-type and GIOP bone. The measurements were done following our previous study (X. Li et al Acta Biomater, 2018; e.g. Supplementary Figure S1 in this reference). We obtain 2D porosity p coefficient of 1.68 (± 0.26)% and 29.57 (± 1.74) % for wild-type and GIOP bone, respectively.

Changes made in text:

We have added a new subsection 2.6 “*Calculation of microscale porosity and stress*” to the *Materials and Methods*, where both the porosity and stress-calculation are discussed. We have also added text

“2.6 Calculation of microscale porosity and stress

The experimental stress data was calculated by the load values divided by the area of the fracture surface, and then corrected by the porosity of bone, following our previous study [15]. SEM image was taken on the fracture surface while the fractured sample was mounted vertically, and the area of the fracture surface was measured from SEM image using ImageJ (NIH, Bethesda, USA). The experimental stress data were post-multiplied by the coefficient $1/(1 - p^{3/2})$ to incorporate the effects – on the effective cross-sectional area – of a 3D isotropic distribution of internal porosity in bone [15]. In this case the 3D porosity is $p^{3/2}$, where p is the 2D porosity coefficient ($p = 2D$ area of voids / 2D bone cross section area), as analysed from backscattered electron (BSE) imaging of the cross section of femoral mid-diaphysis of wild-type and GIOP bone, following our earlier work (Supplementary Information in [15]).

R1-2: How did you calculate tissue level stress? Did you use calipers to determine the cross-section? Or did you do uCT? If so, what was your thresholding? With the increased porosity of the GIOP samples I wonder how accurate your area is when doing measurements and if that might affect your effective modulus values?

AR1-2: The tissue level stress was calculated by the load values divided by the area of the fracture surface, and then corrected by the porosity of bone, following our previous study (L. Xi *et al*, Acta Biomater, 2018). SEM image was taken on the fracture surface while the fractured sample was mounted vertically, and the area of the fracture surface A_0 (i.e. the boundary of the whole tissue-cross section, including the pores) was measured from the SEM image using ImageJ. The corrected effective cross-sectional area is $A_0 (1 - p^{3/2})$.

Changes made in text:

In the new sub-section 2.6 referred to above, we have added the text on stress calculation, highlighted below.

“2.6 Calculation of microscale porosity and stress

The experimental stress data was calculated by the load values divided by the area of the fracture surface, and then corrected by the porosity of bone, following our previous study [15]. SEM image was taken on the fracture surface while the fractured sample was mounted vertically, and the area of the fracture surface was measured from SEM image using ImageJ (NIH, Bethesda, USA). The experimental stress data were post-multiplied by the coefficient $1/(1 - p^{3/2})$ to incorporate the effects – on the effective cross-sectional area – of a 3D isotropic distribution of internal porosity in bone [15]. In this case the 3D porosity is $p^{3/2}$, where p is the 2D porosity coefficient ($p = 2D$ area of voids / 2D bone cross section area), as analysed from backscattered electron (BSE) imaging of the cross section of femoral mid-diaphysis of wild-type and GIOP bone, following our earlier work [15].

R1-3: Does figure 5 have significance bars? Could you add them? Is there a reason these plots look so different from the ones in other figures?

AR1-3: Yes, there are significance bars for the experimental results of the effective fibril modulus, the effective mineral modulus and the fibrillar reorientation rate between WT and GIOP samples tested at different strain-rates in Figure 5, and we add that in the revised figure.

Changes made in text: As above.

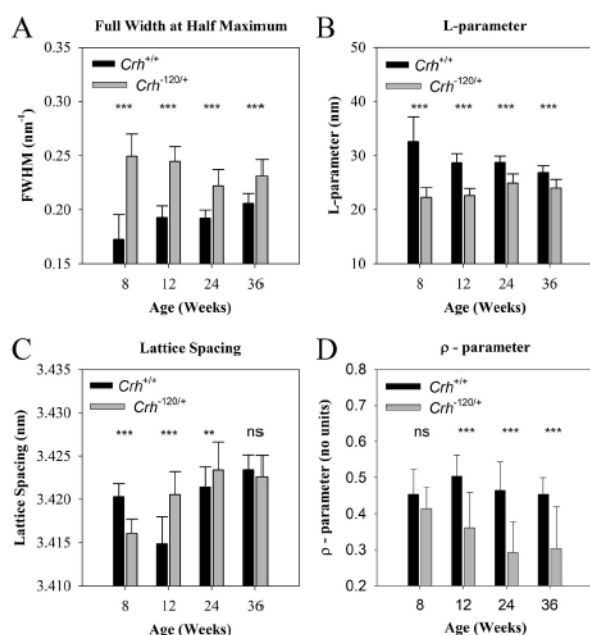
R1-4: In your model, do you ever try varying the collagen and mineral moduli? Both the collagen and the mineral have been shown to change significantly with disease due to substitution and cross-linking. Could GIOP be changing the mechanics of the basic components thus affecting the results?

AR1-4: This is an interesting point. Yes, we did try varying the collagen moduli in our first version of the model (a “biphasic” model, not presented in the paper). In this “biphasic” model, the strain-rate variation was taken to arise solely from the change in mechanics of the collagen phase (a strain-rate stiffening effect), analogous to the strain-rate stiffening of the extrafibrillar matrix (in the current paper).

We found that the biphasic model was not able to capture the change in “effective mineral moduli” at all; indeed, the predicted E_m was nearly constant, in contrast to the experimentally observed increase (Fig 5c). We therefore progressed to the newer version of the model with extrafibrillar matrix stiffening, presented in the paper, which shows better agreement with the three experimental parameters: E_f , E_m , and reorientation.

Our prior work (X. Li et al, Acta Biomater. (2018)) shows that there are small (but significant) differences in mineral crystallographic parameters as well, specifically (002) lattice spacing, FWHM of (002) mineral WAXD peak and L-parameter (from inverse of FWHM). Figure 6 from the paper is

shown below, where Fig. 6A-C shows that the mineral platelet in GIOP bone is slightly shorter than the WT-bone (in length, along the c-axis) and the lattice spacing slightly higher.



However, it is not clear to the current authors how and to what extent these changes in crystallographic structure affect the mineral elastic moduli. As the Reviewer is aware, even in healthy bone maturation the degree of crystallinity, carbonate substitution and other factors alter the local chemical structure of mineral, but the authors do not know of a good model to relate this to mechanical property changes. Perhaps, future *ab initio* molecular dynamics simulations of the change in mineral crystallite structure, linked to simulated mechanical testing at these small scales, could shed light on this question.

Changes made in text:

We have added the following text in the Discussion section:

A limitation of the current work is that we did not report results of varying the collagen- and mineral-moduli in the model, both of which may change in disease due to substitution of ions and change in covalent crosslinking [14, 77]. In this regard, we have observed (data not shown) that variation of collagen moduli cannot explain the increase in effective mineral moduli (Fig 5C) with strain rate. Regarding the mineral phase, our previous study [15] showed that, compared to WT bone, the mineral platelet is slightly shorter (in length, along the c-axis) and the intra-platelet lattice spacing is slightly higher in GIOP bone, but the mechanical implications of these crystallographic changes is not clear to us at this point. Perhaps, future *ab initio* molecular dynamics simulations of the change in mineral crystallite structure [78], linked to simulated mechanical testing at these small scales, could shed light on this question.

Reviewer #2:

This is an interesting article and will make a significant contribution in this special issue of BONE dedicated to J Currey's inspiring life time of work on bone.

The group used the latest gadgets and most up to date testing techniques to get to the very inner structure and deformation of bone at the micro-nanoscale, and argued that on the basis of understanding what is happening at this level one can then grapple with processes acting in the magnification levels above (meso- and macro-structure).

I accept their propositions with a caveat, they are as true as certain assumptions are fulfilled:

R2-1: data produced here is as valid and useful, for human GIOP effects, as far as this mouse model emulates human conditions, if the model does not, so do the results. I SUGGEST the authors make this clear in Abstract, Introduction and Discussion to the reader explicitly stating this very basic underlying assumption.

AR2-1: We agree with the Reviewer that a basic assumption of our work is that the mouse model of endogenous glucocorticoid production (Cushing's syndrome) is a relevant model for human GIOP where exogenous administration of glucocorticoids occurs.

Changes made in text:

Abstract: "... in a murine model of Cushing's syndrome, used to understand steroid-induced osteoporosis...."

Introduction: "published as a model of endogenous GIOP [39]. Prior work has suggested that fracture risk in endogenous glucocorticoid production (Cushing's syndrome) is similar to that in exogenous GIOP [40], although we acknowledge of the limitation of using mouse models to understand human GIOP, due to the absence of secondary osteonal remodelling ..."

Discussion: paragraph 2, end: "...lowered mechanical competence. We note, however, an underlying assumption in our work is that the mouse model of endogenous glucocorticoid production (Cushing's syndrome) is a valid and relevant model for (exogenous) human GIOP [40]. As mouse models do not exhibit secondary remodelling, the bone structure at the tissue level will be different from human GIOP."

R2-2: mouse femurs are extremely slender and thin, as the figure sections themselves show about 200um thin. As such they don't support or allow the very basic model for bone remodelling we know, the best described one and fully prescribed the BMU driven osteonal remodelling. This illustrates the limitations of this model as a valid model for an equivalent human condition. As before I expect the authors to make this clear for the reader, in the 3 main sections in Abstract, Introduction and Discussion.

AR2-2: Please see changes made in response to **R2-1**, where we have included text to this effect.

R2-3: the authors point out that to achieve the SAXS/WAXS they required synchrotron radiation which provides brilliance and high flux. My question is, does this not then also burn (or cook) the collagen during the high strain rate experiments where in order to achieve the data collection the

demand is for the highest acquisition rate and most brilliant illumination? Is there evidence that the bone has not been damaged during these tests?

AR2-3: This appears to be a slight misunderstanding. We did not use “*the most brilliant illumination*” for the high strain-rate tests. We used the **same** X-ray energy level and exposure time per pattern for all WAXD/SAXD patterns collected from samples tested at three different strain rates. In the automated experimental protocol, the beam was blocked (shutter closed) between successive WAXD/SAXD patterns, so the total exposure time for each sample is proportional to the number of patterns per tensile test, which is of the same order of magnitude across strain-rates (accounting for some inter-sample variation). It is, of course, true that the fast strain-rate measurement gets over much quicker, but that is accounted for by varying the “waiting time” from larger to smaller values on increasing the strain-rate.

We added Figure S5 as an example, where it can be seen that the number of patterns per sample is of the same order of magnitude across strain rates. For the examples shown, the sample tested at strain rate of 0.02 s^{-1} actually had *less* exposure time (or number of WAXD/SAXD patterns) than samples tested at strain rate of 0.0004 s^{-1} and 0.01 s^{-1} . Figure S5 is reproduced below.

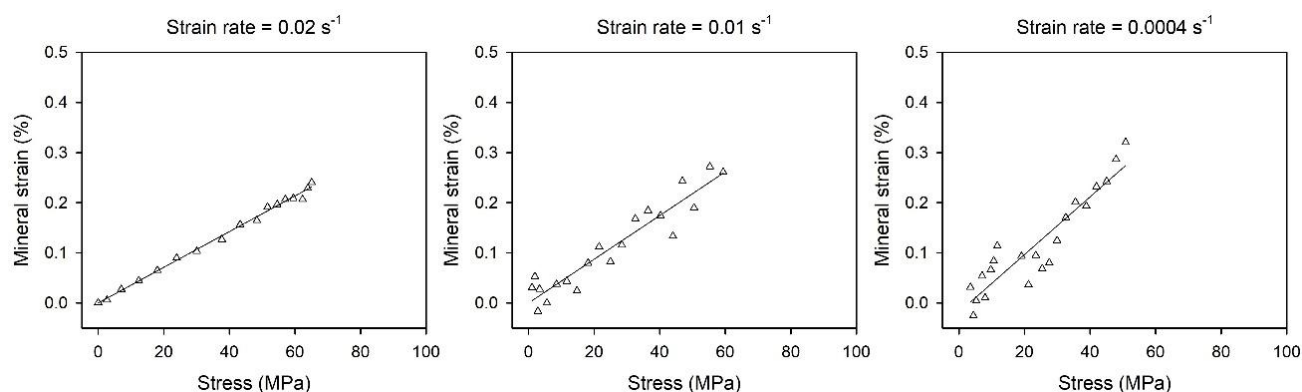


Figure S5: Typical mineral strain versus stress curves for GIOP samples tested at three different strain rates.

We have also added the following text in the Discussion:

“It is noted that the exposure of the samples to X-rays is consistent across three different strain-rates. By closing the shutter between acquisitions, and keeping acquisition time constant at 0.1s per point, the total X-ray dose is proportional to the number of SAXS patterns per tensile test. Figure S5 (Supplementary Information) shows that the number of patterns is of the same order of magnitude across strain-rates. Therefore, it is not likely that the high-strain rate tests are being exposed to much higher X-ray dosages compared to the low- and medium strain-rates, which would cause damage to the collagen matrix [44].”

R2-4: relevance of strain rates: the authors would be advised to specify that only 3 strain rates have been used in this work. Simply rephrasing sentences where their current expression alludes to a wider spread of strain rates, and using instead expressions which make it clear that 3 rates were indeed used, 2 which were near physiological (0.1s, 0.2 s are not high not even intermediate strains rates, simply physiological) and slow (3 orders of magnitude less).

AR2-5: As per the Reviewer's comment, we have rephrased sentences where it may be misinterpreted as a wider spread of strain-rates to be specific to "3" or "three" strain rates. We already had a sentence putting these strain-rates in context in the original MS (section 2.3, para 2).

R2-5: The crux of the results is in Figs 4 & 5. In lines 518-528 the authors describe how wild type bone shows a stiffening with loading rate and re-orientation but also lower maximal strain at $0.1s^{-1}$. Is the behaviour (on the whole) not counter-intuitive when most of us instinctively associate impact and disease with brittle and weak behaviour?

AR2-5: A very interesting observation, thank you. Please note that

i) We considered only data in the elastic regime (before any drops or nonlinearities in the stress/strain curve), so the "lowered maximal strain" is slightly misnamed – it should be lowered maximal strain (in elastic regime).

ii) Further, the lowered strain is at the fibrillar level, and does not account for any interfibrillar, interlamellar or larger-scale strains. Total strain at the tissue/organ level will be a complex sum of these quantities.

iii) Lastly, the maximal (macroscopic) stress is lower for GIOP bone compared to WT, as expected.

When i)-iii) are considered, it can be seen that the expected "weak" (lower strength) behavior in GIOP is still there, while the lower maximal fibril strain in WT- does not exclude that the maximal strain at macroscopic failure (sum of components as in ii)) will still be lower in GIOP than WT (possibly due to tissue-level defects and pores).

Changes made in text:

We have added the following text immediately after the referred text (lines 518-528).

"While the lower maximal fibril strain in WT relative to GIOP sounds counterintuitive when one associates disease with lowered strength and brittleness, we note that a) the total tissue strain is a complex sum of the fibril, interfibrillar, and interlamellar level strains and b) the maximal elastic stress level in GIOP is lower than WT. Therefore, the expected weak (lower strength) behavior in GIOP is present, whilst the lower maximal fibril strain in WT- does not exclude that the maximal strain at macroscopic failure will still be lower in GIOP than WT (possibly due to tissue-level defects and pores)."

R2-6: lines 529-540: the authors make a sincere effort to alert us on the fact that the averaged behaviour does not allow specific effects to be analysed below or above the scale of fibril level magnification. That is all good, but they do not - later on in the ms - clarify how they are proposing to handle the problem (preferably) experimentally. Modelling is not a good recipe, a model is a tool which as good as its connection to a profound reality. If the connection breaks the model fails. I suspect the only unequivocal answer can be derived from an experimental solution to resolve this fibril scale problem, this will then be followed by an improved version of the model.

AR2-6: This is an important point. There needs to be an experimental way to (a) resolve spatial variations in fibrillar structure across the tissue (*above* the individual fibril-scale) and (b) identify the sub-fibrillar level variations (*below* the individual fibril-scale).

For (a), the authors believe newer technological advances in SAXS imaging, for example the 6D SAXS tensor tomography approach [Liebi et al, Nature 2015] can provide full-field maps of the fibrillar structure. Our understanding is that the current bottlenecks in these techniques are in speed of data processing and in potential radiation damage due to excessive exposure in scans + rotations. Advances in these and related-areas may enable spatially-resolved fibrillar-deformation. However dynamic and very rapid deformation studies will be still challenging.

For (b), with current techniques it would be suitable to model the covariation of angular intensity of the WAXD diffraction signal (from mineral) with the SAXS signal, which can provide some information on molecular-scale deformation of the mineral in relation to the fibrils. We are working on this. Another route would be to use contrast-variation neutron scattering to identify the molecular-level diffraction from collagen (we are not experts in this area, and size of beam relative to the sample may be an issue) and link to the fibril SAXS pattern. This would potentially give information on intrafibrillar rearrangement and dynamics. Also, the 6D and tensor tomography methods in a) can also be applied here.

Changes made in text:

At the end of the Discussion paragraph, starting “Fibrillar reorientation, as well, ...”

“To be able to overcome the averaging issue inherent in our experimental configuration, possible future routes may involve 6D SAXS tensor tomography [71], if challenges in data processing and potential radiation damage are overcome. Such methods can provide spatially-resolved 3D maps of the fibrillar nanostructure across the tissue, although time-resolved studies at the strain-rates proposed here (and above) will still be challenging. Subfibrillar-level deformation may be analyzed by the covariation of changes in the angular intensities of the WAXD and SAXS patterns (which will provide information on how the mineral particles are reorienting relative to the fibrils), or possibly by contrast-variation neutron diffraction to resolve the changes in tropocollagen ordering.”

R2-7: .. line 539: as noted by the authors), so it is not likely that this second effect is playing a major role. "it is not likely" is this not an important assumption which needs some justification?

AR2-7: Yes, this was too terse in the original text. We overlooked to add additional sentences here which would have provided clearer justification.

In brief, the effective tilt angle (Figure 2 in Orgel et al (2006)) of the tropocollagen molecules are (estimate from the figure) about 4° (noting the factor of 5 compression in the c-axis direction specified by the authors). This value is much smaller (Figure 5D) compared to the ~50° (FWHM change)/% strain reorientation seen for the lowest strain rate. Therefore, load-induced intrafibrillar rotation of the molecules, to remove the tilt, would be insufficient to explain the magnitude of the observed reduction in FWHM.

Changes made in Text:

We have added the above text as a replacement for the existing single sentence (Discussion paragraph 4).

“... However, we note that the numerical value of the tilt inside microfibrils is small ($\sim 4^\circ$ in Figures 2-3 in [70]) (noting the factor of 5 compression in the c-axis direction specified by the authors). This value is much smaller (Figure 5D) compared to the $\sim 50^\circ$ (FWHM change)/% strain reorientation seen for the lowest strain rate. Therefore, load-induced intrafibrillar rotation of the molecules, to remove the tilt, would be insufficient to explain the magnitude of the observed reduction in FWHM. ...”

TYPOS:

80_ ... properties of bone was pioneered by John Currey

85- ... mechanical performance under three different loading speeds.

92- ... scale[12, 13] and further aggregate into trabecular and cortical

112- ... Glucocorticoids suppress bone formation through inducing osteoblast and osteocyte apoptosis and the inhibition of proliferation ...

115- ... osteoblastogenesis, but toward adipogenesis....

119- ... Glucocorticoids directly affect osteoclasts resulting in decreased osteoclast apoptosis and increased osteoclast formation of a prolonged life span, which explains the observed enhanced and prolonged bone resorption [27]....

122-... Although excess of glucocorticoids leads to an increased osteoclast number, osteoclast function may be affected too, with impaired spreading and resorption of mineralized matrix. The osteoblast signals could also be impaired due to the abnormal osteoclast function [28].

136-... to controls [31].

145-... In this study, we examine the deformation of the mineralized fibrils in the bone matrix of a GIOP mouse model at 3 different strain rates ...

156-... fixed age point (24 weeks) and at 3 strain rates to quantify the alterations

Changes made in Text:

Thank you for identifying these typos. As above, all typos were corrected in the revised paper.

Highlights – key findings

- Mineralized fibrils in healthy mouse bone show strain-rate dependent stiffening.
- The fibrillar stiffening is absent in steroid-induced osteoporosis.
- Modelling suggests altered collagen-mineral interactions may explain this change.
- Changed fibrillar stiffening may be relevant to altered mechanics in osteoporosis.

Reduction of fibrillar strain-rate sensitivity in steroid-induced osteoporosis linked to changes in mineralized fibrillar nanostructure

L. Xi^{*a,b}, P. De Falco^{*b,c}, E. Barbieri^{b,d}, A. Karunaratne^e, L. Bentley^f, C.T. Esapa^{f,g}, G.R. Davis^m, N.J. Terrill^h, R.D. Cox^f, N. M. Pugno^{j,b,k}, R.V. Thakker^g, R. Weinkamer^c, W.W. Wu^{a,#}, D.N. Fang^{a,l} and H.S. Gupta^{b,#}

a. Institute of Advanced Structure Technology, Beijing Institute of Technology, Beijing 100081, China

b. School of Engineering and Material Sciences, Queen Mary University of London, London, E1 4NS, UK

c. Department of Biomaterials, Max Planck Institute of Colloids and Interfaces, D-14424 Potsdam-Golm, Germany

d. Department of Mathematical Science and Advanced Technology (MAT), Yokohama Institute for Earth Sciences (YES) 3173-25, Showa-machi, Kanazawa-ku, Yokohama-city, Japan

e. Department of Mechanical Engineering, University of Moratuwa, Sri Lanka

f. MRC Mammalian Genetics Unit and Mary Lyon Centre, MRC Harwell, Harwell Science and Innovation Campus, OX11 0RD, UK

g. Academic Endocrine Unit, Radcliffe Department of Clinical Medicine, Oxford Centre for Diabetes, Endocrinology and Metabolism (OCDEM), University of Oxford, Churchill Hospital, Headington, Oxford, OX3 7JL, UK

h. Beamline I22, Diamond Light Source Ltd., Diamond House, Harwell Science and Innovation Campus, Chilton, Didcot, Oxfordshire, OX11 0DE, United Kingdom

j. Laboratory of Bio-Inspired & Graphene Nanomechanics, Department of Civil, Environmental and Mechanical Engineering, University of Trento, Via Mesiano, 77, 38123, Trento, Italy

k. Ket Lab, Edoardo Amaldi Foundation, Via del Politecnico snc, 00133, Rome, Italy

l. State Key Laboratory for Turbulence and Complex Systems, College of Engineering, Peking University, Beijing, China

m. Dental Physical Sciences Unit, Queen Mary University of London, London, E1 4NS, UK

*. These authors contributed equally to this work.

#. Correspondence authors

E-mail addresses: xili@bit.edu.cn (L. Xi), paolino.defalco@mpikg.mpg.de (P. De Falco),

e.barbieri@jamstec.go.jp (E. Barbieri), angelok@uom.lk (A. Karunaratne), l.bentley@har.mrc.ac.uk (L.

Bentley), c.esapa@har.mrc.ac.uk (C.T. Esapa), g.r.davis@qmul.ac.uk (G.R. Davis),

nick.terrill@diamond.ac.uk (N.J. Terrill), r.cox@har.mrc.ac.uk (R.D. Cox), nicola.pugno@unitn.it (N. M.

Pugno), rajesh.thakker@ndm.ox.ac.uk (R.V. Thakker), richard.weinkamer@mpikg.mpg.de (R. Weinkamer),

wuwenwang@bit.edu.cn (W.W. Wu), fangdn@bit.edu.cn (D.N. Fang), h.gupta@qmul.ac.uk (H.S. Gupta).

#Correspondence author:

Himadri S. Gupta, h.gupta@qmul.ac.uk

School of Engineering and Materials Sciences and Institute of Bioengineering,

Queen Mary University of London, Mile End Road, London E1 4NS, UK

Tel: +44(0)20 7882 8867

Wenwang Wu, wuwenwang@bit.edu.cn

Institute of Advanced Structure Technology, Beijing Institute of Technology

Beijing 100081, China

Significance Statement

44 Biomechanically bone undergoes different loading-rates, from low (standing) to high (rapid loading
45 during fracture), and its mechanical response varies with strain-rate. However, the role of the
46 mineralized fibrillar matrix in contributing to the change in mechanical response is incompletely
47 understood. In particular, the changes in bone matrix strain-rate sensitivity during metabolic bone
48 disorders like osteoporosis are little studied. Here, we use rapid synchrotron X-ray imaging during
49 variable strain-rate tests on cortical bone from a murine model of steroid-induced osteoporosis, to
50 study the matrix-level response. We find that while control-samples showed an increase in effective
51 fibrillar and mineral modulus with strain-rate, this effect is completely suppressed in osteoporotic
52 bone. We model this effect by considering the matrix as a two-level fibrillar/lamellar composite, and
53 find that the changes may be explained by an altered interaction between the collagen and mineral at
54 the nanoscale. Our results suggest that an altered strain-rate sensitivity of the bone matrix in
55 osteoporosis may be one of the contributing factors to reduced mechanical competence in such
56 metabolic bone disorders.

59 **Abstract**

1
60 As bone is used in a dynamic mechanical environment, understanding the structural origins of its
61 time-dependent mechanical behaviour – and the alterations in metabolic bone disease – is of interest.
62 However, at the scale of the mineralized fibrillar matrix (nanometre-level), the nature of the strain-
63 rate dependent mechanics is incompletely understood. Here, we investigate the fibrillar- and mineral-
64 deformation behaviour in a murine model of **Cushing's syndrome, used to understand** steroid
65 induced osteoporosis, using synchrotron small- and wide-angle scattering/diffraction combined with
166 *in situ* tensile testing **at three strain rates ranging from** 10^{-4} to 10^{-1} s^{-1} . We find that the effective
167 fibril- and mineral-modulus and fibrillar-reorientation show no significant increase with strain-rate in
168 osteoporotic bone, but increase significantly in normal (wild-type) bone. By applying a fibril-
169 lamellar two-level structural model of bone matrix deformation to fit the results, we obtain
170 indications that altered collagen-mineral interactions at the nanoscale – along with altered fibrillar
171 orientation distributions – may be the underlying reason for this altered strain-rate sensitivity. Our
172 results suggest that an altered strain-rate sensitivity of the bone matrix in osteoporosis may be one of
173 the contributing factors to reduced mechanical competence in such metabolic bone disorders, and
204 that increasing this sensitivity may improve biomechanical performance.
21
22
23
24
25
26
27
28
29
30
31
32
33
34
35
36
37
38
39
40
41
42
43
44
45
46
47
48
49
50
51
52
53
54
55
56
57
58
59
60
61
62
63
64
65

1 Introduction

Determining the mechanically-critical structural and compositional alterations of bone matrix in metabolic bone disorders, such as osteoporosis or osteogenesis imperfecta, is essential to understand origins of the reduced mechanical competence exhibited in such disorders [1-3]. A systematic characterization of the mechanical properties of bone was pioneered by John Currey [4]. Among his many contributions to biomechanics, he found that stiffness, strength and toughness of bone depend on biological factors such as anatomical specialisation [5] and species [6], as well as on factors related to materials-composition and structure, such as mineral [7] and collagen content [8, 9]. The research presented here was performed in the spirit of his systematic approach, but focusses not on quasi-static mechanical properties, but on changes of the mechanical performance under three different loading speeds. As bone is used under time-dependent loading in a dynamic mechanical environment, linking the viscoelastic and strain-rate dependent behaviour of bone matrix to such alterations is important. However, clinical measures assessing bone state (such as bone mineral density (BMD)) capture mainly changes in bone mass, and provide little information on alterations in quality of the bone matrix. The matrix of bone at the nanoscale is a composite of Type-I collagen fibrils, carbonated apatite, noncollageneous proteins and water [10, 11], which are assembled into fibre-arrays at the micron-scale [12, 13] and further aggregate into trabecular and cortical bone types to form the organ bone [5]. Metabolic bone diseases may affect not only the macro- and microscale structure of bone, but also change the bone matrix-level quality [2], via altered cellular modelling and remodelling cycles. Alterations in matrix quality, such as collagen-cross linking [8, 9, 14] mineral-platelet structural changes [15] and the expression of noncollageneous proteins like osteopontin [16], have been shown to lead to deterioration or alteration in macroscopic mechanical properties, but the details of the nanoscale mechanisms are not completely understood. Understanding the nanostructural response of bone matrix to time-dependent loading in bone-disease types like osteoporosis is therefore of importance both to basic medical science as well as, eventually, to clinical practice.

In this regard, glucocorticoid induced osteoporosis (GIOP) is a prototypical secondary osteoporosis where BMD is known to be insufficient to explain mechanical changes. As the most common form of secondary osteoporosis, GIOP affects 1-3% of the general population and results in severe morbidity, especially in post-menopausal women and older men [17, 18]. GIOP usually develops in patients receiving glucocorticoids for the treatment of a variety of diseases like inflammatory and autoimmune disorders, and these underlying diseases themselves can also have negative effects on bone metabolism which constitute a risk of osteoporosis [19]. Glucocorticoids treatment results in

109 altered bone remodelling, early and rapid bone loss and increased fracture risk, through direct effects
110 on bone cells and indirect effects through alteration of the neuromuscular system and gonadal
111 hormones [20]. As a crucial process in GIOP, reduced bone volume is caused by osteoclastic activity
112 (bone resorption) that cannot be matched by osteoblastic activity (bone formation) [21, 22].
113 Glucocorticoids suppress bone formation through inducing osteoblast and osteocyte apoptosis and
114 the inhibition of proliferation, differentiation, maturation and activity of osteoblasts [23]. In the
115 presence of glucocorticoids, the osteoblast precursor cells (mesenchymal cells) in bone marrow are
116 not differentiated or directed toward osteoblastogenesis, but toward adipogenesis (cells of the
117 adipocytic lineage) [24]. Glucocorticoids inhibit the differentiation of osteoblasts by a mechanism of
118 opposing *Wnt*/ β -catenin pathway, and *Wnt* signalling plays a critical role in increasing bone mass
119 through induction of differentiation of bone-forming cells (osteoblasts), inhibition of osteoblast and
120 osteocyte apoptosis, and suppression of the development of bone-resorbing cells (osteoclasts) [25,
121 26]. Glucocorticoids directly affect osteoclasts resulting in decreased osteoclast apoptosis and
122 increased osteoclast formation of a prolonged life span, which explains the observed enhanced and
123 prolonged bone resorption [27]. The proliferation of osteoclasts is inhibited by glucocorticoids in a
124 dose dependent manner. Although excess of glucocorticoids leads to an increased osteoclast number,
125 osteoclast function may be affected too, with impaired spreading and resorption of mineralized
126 matrix. The osteoblast signals could also be impaired due to the abnormal osteoclast function [28].

127 However, the way these biological changes in GIOP affect the nano- and microscale mechanics is
128 incompletely understood, especially in the area of time-dependent loading. Previous studies have
129 showed that glucocorticoid therapy affects not only the amount of bone (bone quantity) but also the
130 micro-architecture and other material level properties (bone quality) [17, 29, 30]. Micro-CT studies
131 of trabecular and cortical bone with glucocorticoids treatment showed reduced trabecular bone
132 volume, trabecular connectivity, trabecular number and cortical thickness as compared to control
133 group [31, 32]. Glucocorticoid-treated mice showed increased size of osteocyte lacunae and there are
134 “halos” of hypomineralized bone surrounding the lacunae, with corresponding reduced (~40%)
135 mineral to matrix ratio as measured by Raman microspectroscopy. A reduction in mineral
136 concentration (by 45%) caused by glucocorticoids treatment is accompanied by reduced degree of
137 bone mineralization, as compared to controls [31]. Our previous study on a mouse model of
138 endogenous hypercorticozonaemia (Cushing's syndrome) shows a significant reduction (by 51%)
139 of fibril modulus, larger fibril strain/tissue strain ratio and a disruption of intracortical architecture as
140 compared with their wild-type littermates [33]. In relation to mechanics, bone fractures in healthy
141 individuals usually happen with traumatic events at high strain rates, whereas in GIOP, bones are

142 additionally involving fragility fractures with minimal trauma at relatively low strain rates [1, 34, 35].
143 Since the quasi-static fibrillar-level mechanics and structure are altered in GIOP-bone [15, 33], it is
144 therefore of interest to investigate, in this prototypical secondary osteoporosis, possible viscoelastic
145 and strain-rate dependent effects in the mineralized fibrillar matrix.

146 In this study, we **examine** the deformation of the mineralized fibrils in the bone matrix of a GIOP
147 mouse model **at three different strain rates**, using high-brilliance time-resolved synchrotron small-
148 angle X-ray scattering (SAXS) and wide-angle X-ray diffraction (WAXD). These X-ray techniques
149 provide information on the fibrillar- and mineral platelet-level strain in the bone matrix, induced by
150 external mechanical loads. When combined with a high brilliance synchrotron source, SAXS/WAXD
151 measurements can be carried out with time-resolution of the order of seconds [14, 15, 36-38],
152 facilitating dynamic measurements. For the animal model of GIOP, we use a mouse model (*Crh*^{-120/+})
153 of endogenous hypercorticozonaemia (Cushing's syndrome), published as a model of endogenous
154 GIOP [39]. **Prior work has suggested that fracture risk in endogenous glucocorticoid production**
155 **(Cushing's syndrome) is similar to that in exogenous GIOP [40], although we acknowledge of the**
156 **limitation of using mouse models to understand human GIOP, due to the absence of secondary**
157 **osteonal remodelling.** Our previous quasi-static (not time-dependent) SAXS/WAXD study, on the
158 developmental changes in bone nanostructure in this model, provided evidence for increased fibrillar
159 deformability, more random fibrillar orientation, and shorter/less stress-reinforcing mineral platelets
160 in GIOP [15, 33]. Here, we carry out tensile deformation on cortical GIOP mouse bone at a fixed age
161 point (24 weeks) and **at three strain rates to** quantify the alterations in fibrillar mechanics in
162 comparison to wild-type animals. Because SAXS/WAXD measurements are intrinsically volume-
163 averaged measures of nanoscale deformation, the experimental data is combined with a multiscale
164 model of the mechanics of the fibrils and fibril-arrays, developed from previous work [13, 36, 41], to
165 help in the interpretation of the experimental results.

166 **2 Materials and Methods**

167 **2.1 Animals**

168 Bone tissue from female GIOP mice (*Crh*^{-120/+}) and wild-type (*Crh*^{+/+}) littermates on a C57BL/6
169 genetic background (3rd generation) aged 24 weeks were used in this study. Mouse samples were
170 stored at -20 °C before experiments. The mice were bred as part of a prior study [39], where all
171 animal studies were carried out using guidelines issued by the UK Medical Research Council, in
172 Responsibility in Use of Animals for Medical Research (July 1993) and Home Office Project
173 License numbers 30/2433 and 30/2642.

174 **2.2 Sample preparation for *in situ* tensile testing**

1
2
175 Murine femora were dissected and longitudinally sectioned along the long axis using a water-
3
176 irrigated low speed saw with a diamond-coated blade. The distal and proximal ends of anterior
4
177 femora strips were embedded in dental ionomer (FiltekTM Supreme XT, 3M ESPE, USA) such that
5
178 samples could be mounted in the microtensile tester. The dental ionomer was exposed in UV light
6
179 for 20 s, while the mid-diaphysis of femora bone was covered by lead tape during UV light exposure
7
180 to prevent any UV-induced tissue alteration. The obtained femora strips for microtensile testing have
8
181 typical gauge length, width and thickness of 5 mm, 1 mm and 0.2 mm, respectively. Samples were
9
182 then wrapped in PBS-soaked tissue paper and stored at - 20 °C before used for mechanical testing.
10
11
12
13
14
15
16
17

183 **2.3 *In situ* micro tensile testing with simultaneous synchrotron SAXD/WAXD measurements**

18
19
20
21
22
23
24
25
26
27
28
29
30
31
32
33
34
35
36
37
38
39
40
41
42
43
44
45
46
47
48
49
50
51
52
53
54
55
56
57
58
59
60
61
62
63
64
65

Combining *in situ* tensile testing with real time synchrotron SAXD and WAXD, the load data (from load cell), fibril strain ϵ_f (from the SAXD frames) and mineral strain ϵ_m (from the WAXD frames) can be collected concurrently, as initially devised by Gupta et al. [37]. A customized microtensile tester was mounted in the path of synchrotron X-ray beam at beamline I22, Diamond Light Source (Harwell, UK), such that SAXD and WAXD frames were collected concurrently with mechanical loading of the sample. Samples were uniaxially loaded in tension using a customized microtensile tester equipped with a DC linear-encoder stage (M112.1DG; Physic Instruments, UK) and an 111N model SLC31/00025 tension/compression load cell (RDP Electronics Ltd, UK). A custom LabVIEW based software (LabVIEW 2013, National Instruments, UK) was used to control the microtensile tester and CCD camera. Samples were tested at room temperature and hydrated throughout each experiment in a fluid bath filled with physiological saline (PBS solution).

For the three different load rates used in the current study, the motor velocities were set to be 0.1, 0.05 and 0.002 mm/s, which corresponding to motor strain rates of 0.02 s⁻¹, 0.01 s⁻¹ and 0.0004 s⁻¹, respectively. Strain rates of 0.02 s⁻¹ and 0.01 s⁻¹ were used because they are in the range of physiological strain rates during walking and running, whereas a strain rate of 0.0004 s⁻¹ representing the quasi-static loading was also examined as strain rates near this magnitude have been used in our previous studies [15, 33, 42, 43]. The numbers of samples tested at strain rate of 0.02 s⁻¹, 0.01 s⁻¹ and 0.0004 s⁻¹ were 4, 4 and 4, respectively, for wild-type mice; and 6, 5 and 4, respectively, for GIOP mice.

For the synchrotron SAXD and WAXD measurement, the X-ray wavelength λ was 0.8857 Å and beam cross section was ~240 × 80 μm at the sample. A Pilatus P3-2M detector was used to collect the SAXD data, while a Pilatus P3-2M-DLS-L detector was used to collect the WAXD data; both

206 detectors have a pixel resolution of 1475 x 1679 pixels and pixel size of 172 x 172 μm^2 . Note that in
207 the concurrent SAXD/WAXD measurement protocol used, one quadrant (lower right) of the WAXD
208 detector space is removed to allow for the remaining SAXD signal to transmit to the downstream
209 SAXD detector; as a result, the WAXD pattern spans 3 out of 4 quadrants on the detector. The
210 sample-to-detector distance was ~ 3727.0 mm for SAXD detector and ~ 175.3 mm for WAXD
211 detector, as measured with Silver Behenate and Silicon standard, respectively. The X-ray exposure
212 time was 0.1 s for both SAXD and WAXD patterns for samples measured at all strain rates. Due to
213 the different durations of the mechanical tests at different strain-rates, the period between successive
214 SAXD/WAXD acquisitions (with beam shutter closed) was controlled by the wait-time parameter
215 (0.1 s: strain rate 0.01 s^{-1} and 0.02 s^{-1} , and 3.4 s: strain rate of 0.0004 s^{-1}). The beam shutter was
216 closed between consecutive acquisitions of SAXD and WAXD patterns, to minimise the effect of X-
217 ray irradiation on the mechanical properties of bone tissue [44].

218 2.4 SAXD and WAXD data analysis

219 Fibril strains and load-induced changes in fibrillar orientation distribution were measured from 2D
220 SAXD patterns, and mineral strains were measured from 2D WAXD patterns.

221 **Fibril strain:** The meridional stagger (D-period) of collagen molecules inside the fibril leads to an
222 axial diffraction pattern in the small-angle region of reciprocal space [45]. The third-order
223 meridional collagen reflections were used to measure the D-period of collagen fibrils evaluating a
224 radially-narrow semi-circular sector (180° angular width) (**Figure 1G**); this corresponds to
225 considering an integrated averaged of fibrillar deformation in all directions. The fibril strain (ϵ_f) was
226 calculated from the percentage increases in D-period during tensile testing of samples [15, 33, 45,
227 46]. SAXD patterns at different stress levels are shown in the *supplementary information* (**Figure**
228 **S1**).

229 **Mineral strain:** For WAXD, the mineral particles consist of apatite (with a lattice structure of
230 hexagonal closed-packed or *hcp* type) with the *c*-axis predominantly oriented along the fibril
231 direction [47]. In a similar manner to the SAXD analysis, the mineral strain (ϵ_m) along the loading
232 direction was measured from the percentage changes of lattice spacing, obtained from the (002) peak
233 centre position of apatite averaged in a radially-narrow semi-circular (180° angular width) in the
234 upper quadrant, in an analogous manner to SAXD (**Figure 1E**), similar to prior work [14, 15, 38, 45].
235 The *Processing* perspective of the data analysis software package DAWN [48] (www.dawnsci.org)
236 was used for SAXD and WAXD data reduction. The integrated SAXD and WAXD 1D intensity

237 profiles (**Figure 1F and H**) were obtained from 2D SAXS/WAXD images as described above.
238 Subsequently, the 1D profiles were fitted using a custom Python script. Both the 1D collagen SAXD
239 data and the 1D mineral WAXD data were fitted to combinations of a Gaussian peak and a linear
240 background term. To analyse the change of fibril and mineral strains during tensile loading, the
241 obtained peak centre positions were used to calculate the D-period for the collagen fibrils and the
242 (002) crystallographic lattice spacing for the mineral apatite. Linear regressions of D-period and
243 D(002) were carried out versus macroscopic stress, and the intercept of each regression was taken as
244 the unstrained (zero-stress) value for D-period and D(002). The collagen fibril strains ϵ_f and mineral
245 strains ϵ_m were calculated from the percentage changes of collagen D-period and the (002) lattice
246 spacing, respectively, relative to the unstrained state. The *effective fibril modulus* ($E_f = d\sigma/d\epsilon_f$) and
247 *effective mineral modulus* ($E_m = d\sigma/d\epsilon_m$) were defined as the slope of tissue-level stress σ versus
248 fibril strain and mineral strain, respectively, from the elastic region of deformation (**Figure S3-4,**
249 **supplementary information**), as described in prior work [15, 33, 45]. We note that the terminology
250 (effective fibril modulus and mineral modulus) is used for consistency with prior work [15, 33, 49],
251 and as will be discussed in the modelling section, these parameters are not equivalent to the actual
252 fibril and mineral elastic modulus (hence the use of the qualifier “effective”).

253 **Fibrillar orientation distribution:** The changes in fibrillar orientation distribution with tensile load
254 were analysed by observing the narrowing of the FWHM of the angular variation of SAXD intensity
255 of the first-order collagen reflection, as described in our prior study on quasi-static deformation of
256 glucocorticoid-induced osteoporotic bone [33]. Using the DAWN processing perspective, radially
257 averaged azimuthal intensity profiles $I(\chi; q_0)$ were calculated over the full azimuthal range (360°)
258 from the first-order collagen reflection (at $q = q_0 = 6\pi/D$). To subtract out the diffuse scattering
259 background due to the mineral, similar azimuthal intensity profiles $I_m(\chi; q_0 - \Delta q)$ and $I_m(\chi; q_0 + \Delta q)$
260 near the first-order collagen reflection, with $\Delta q = 0.015 \text{ nm}^{-1}$ chosen to have $q_0 \pm \Delta q$ outside of the
261 first-order collagen peak, were calculated and averaged. The corrected azimuthal intensity profile I_c
262 (χ) was calculated as $I_c(\chi) = I(\chi; q_0) - 0.5 \times [I_m(\chi; q_0 - \Delta q) + I_m(\chi; q_0 + \Delta q)]$. The obtained $I_c(\chi)$ was
263 fitted with a pair of Gaussian peak functions separated by 180° . From the fit, the peak position
264 indicates the predominant direction of fibril orientation, while the peak width (FWHM) is related to
265 the extent of fibrillar alignment: larger FWHMs correspond to lower alignment (See **Figure S2** in the
266 **supplementary information**). The rate of fibrillar reorientation was calculated from the slope of
267 FWHM (degrees) versus fibril strain (%) curve for each sample [33], with units of degrees/%.

268 2.5 X-ray microtomography

269 X-ray microtomography was used to study 3D micromorphometry and microscale mineralization
270 distribution of bone tissue. Mice femora were longitudinally sectioned into two halves. Five samples
271 from both wild-type and GIOP mice were used for X-ray microtomography measurements to obtain
272 tomograms, which were used for quantitative analysis of microscale mineralization distribution in
273 femoral mid-shaft from both wild-type and GIOP mice. Samples were mounted on the sample stage
274 of a high-definition X-ray microtomography scanner (MuCat scanner) which equipped with an
275 ultrafocus X-ray generator (Nikon Metrology (Leuven, Belgium)) and CCD camera (Spectral
276 Instruments Inc (Tucson, Arizona, USA)) in a time-delay integration readout mode. An accelerating
277 voltage of 40 kV was used to scan mice femora samples and a voxel size of $15 \times 15 \times 15 \mu\text{m}^3$ was
278 obtained. The projection data were processed following a calibration procedure, in which the
279 scanning data were corrected to an equivalence of 25 keV monochromatic X-ray source, and then a
280 reconstruction procedure in which a cone-beam back-projection algorithm was used to generate 3D
281 images (representing the absolute linear attenuation coefficient at 25 keV) of the scanned regions of
282 samples. The 3D tomograms of samples were processed with an in-house software (Tomview,
283 authored by GRD) to export a series of 8-bit grey level slices, multiplying the linear attenuation
284 coefficient by a known constant to obtain an appropriate dynamic range. The histograms of grey
285 levels for wild-type mice and two distinct regions of interest in GIOP mice - periosteal region and
286 endosteal region (**Figure 2 C1**)- were generated from 2D slices using ImageJ software (ImageJ, NIH,
287 USA). The histograms of grey levels for three data groups were converted into histograms of mineral
288 concentration using published X-ray attenuation data [50], from which the average mineral
289 concentrations (denoted as the degree of mineralisation) measured as hydroxyapatite (g/cm^3) were
290 calculated and plotted for different bone regions (**Figure 2E-F**). The mineral concentration is
291 converted to mineral volume fraction as previously described [51, 52]. For input of experimental
292 mineral concentrations into the model (described below), the mineral concentration and volume
293 fraction are taken as the average values across the cross-section of the tissue, similar to our prior
294 work [15].

2.6 Calculation of microscale porosity and stress

The experimental stress data was calculated by the load values divided by the area of the fracture surface, and then corrected by the porosity of bone, following our previous study [15]. SEM image was taken on the fracture surface while the fractured sample was mounted vertically, and the area of the fracture surface was measured from SEM image using ImageJ (NIH, Bethesda, USA). The experimental stress data were post-multiplied by the coefficient $1/(1 - p^{3/2})$ to incorporate the effects – on the effective cross-sectional area – of a 3D isotropic distribution of internal porosity in bone

302 [15]. In this case the 3D porosity is $p^{3/2}$, where p is the 2D porosity coefficient ($p = 2D$ area of voids /
303 2D bone cross section area), as analysed from backscattered electron (BSE) imaging of the cross
304 section of femoral mid-diaphysis of wild-type and GIOP bone, following our earlier work
305 (Supplementary Information in [15]).

306 2.7 Statistical analysis

307 To test for statistical differences in bone mineralization and the nanoscale mechanical deformation
308 behaviour between samples tested at **three** different strain-rates, one-way ANOVA tests with all
309 pairwise multiple comparison procedures (Holm-Sidak method) were performed on the experimental
310 measured results including the mean mineral concentration, the effective fibril modulus, the effective
311 mineral modulus and the fibrillar reorientation rate. SigmaPlot (Systat Software Inc., USA) was used
312 for the statistical analysis. The statistical significances were denoted on the figures (*: $p < 0.05$, **: p
313 < 0.01 , ***: $p < 0.001$, ns: not significant for $p > 0.05$).

314 2.8 Modelling of fibrillar and lamellar mechanics

315 To understand the structural mechanisms underpinning trends in E_f , E_m and fibrillar reorientation
316 with strain-rate, we develop a two-level hierarchical model of the fibrils and fibril arrays, based on
317 prior work, which is briefly summarized below (details in Supplementary Information). Analytical
318 fitting (performed in *Matlab* [53]) and numerical (finite element) simulations performed in *Abaqus*
319 *6.14* [54] are used to fit the model to data. The experimental parameters are fitted to equivalent
320 model parameters, summarized in the two columns of **Table 1**.

322 **Table 1: Description of the moduli introduced for the study of the bone mechanical properties at**
 323 **different length scales and of the fibrillar reorientation phenomenon.** The term ‘effective’ indicates
 324 that the moduli result from the ratio of terms computed at different length scales. Specifically, they
 325 are calculated from the ratio of stresses applied at the macroscale and of strains computed at the
 326 microscale (effective fibril modulus) and at the nanoscale (effective mineral modulus). The equations
 327 used for the analytical calculation of these parameters are listed in Supplementary Information,
 328 Equations S1-S6. ‘*afs*’ is the average fibril strain, φ_{EM} is the volume fraction of the extrafibrillar
 329 matrix and *k* is a factor defined in Equation S6.

Nomenclature of the modulus	Experimental	Analytical/Numerical
Effective fibril modulus	$\frac{\text{Applied tissue stress}}{\text{average fibril strain}}$ Calculated via linear fitting of experimental data shown in Figure 5A .	$\frac{\text{Applied laminate stress}}{\text{average strain of the sublamellae}}$ Computed via laminate theory.
Effective mineral modulus	$\frac{\text{Applied tissue stress}}{\text{mineral strain}}$ Calculated via linear fitting of experimental data shown in Figure 5B .	$\frac{\text{Applied tissue stress}}{(afs * \varphi_{EM}) + (afs * \frac{(1 - \varphi_{EM})}{k})}$ Computed via laminate theory.
ΔFWHM/fibril strain	Δ FWHM: variation of the FWHM of Gaussian fitting ‘I vs χ ’ curves (more details in Supplementary Information). Fibril strain: average fibril strain, averaged from the volume of bone (beam size * sample thickness) measured by x-ray.	Δ FWHM: variation of the FWHM of the lamellar angular distribution (Gaussian distribution). The fibrillar reorientation leading to this variation was computed via FE simulations. Fibril strain: average strain of the sub-lamellae (computed via laminate theory).

2.9 Model structure and parameters

2.9.1 Analytical relations

Nanoscale force-balance relations: Stresses and strains on the fibril, mineral platelet and extrafibrillar matrix were calculated by considering the fibril as a staggered array of mineral particles embedded with a collagen matrix (**Figure 3A-I**), which is in turn embedded in an extrafibrillar matrix. The model follows earlier work on staggered model architecture of the mineralized fibrils in bone and related biomineralized tissues [11, 36, 41, 55-57]. The mineral platelet aspect ratio was taken as 15 and 9.6 respectively for the wild-type and GIOP models, following our prior ultrastructural determination of mineral structure (L -parameter) using WAXD on GIOP- and WT-bone from the same cohort at a similar age-point [15]. A second parameter of note in the staggered model is the k -factor, which is inversely related to the stress transferred to the mineral via shear in the collagen matrix [11, 36]. Mineral and collagen were taken as elastic, and the strain-rate sensitivity was incorporated into the material response of the extrafibrillar matrix, whose constitutive law was taken as the Ramberg-Osgood law $\varepsilon = \sigma / (c \dot{\varepsilon}^d)$ [58, 59]. Most parameters were obtained from referenced literature (**Table 2**), with the exception of the Young's modulus and volume fraction of the extrafibrillar matrix, and the k -factor, which are obtained from nonlinear fitting to the experimental data (**Figure S6**) and will be reported in the **Results**. The tissue mineral volume fraction values were taken from the 24-week time-point values of volume fraction in GIOP- and WT-mice, in our recent work [15], with $\varphi_m = 0.40$ for GIOP and $\varphi_m = 0.45$ for WT.

Plywood structural parameters: The bone lamella was modelled as a set of differently oriented fibril layers, with angular orientations at 0° , $\pm 5^\circ$, $\pm 10^\circ$, $\pm 15^\circ$, $\pm 30^\circ$, $\pm 45^\circ$, $\pm 60^\circ$, $\pm 75^\circ$ and 90° . To determine the relative thicknesses of each layer, these were varied till the FWHM of the simulated fibril orientation distribution matched the experimental azimuthal intensity distribution of the meridional collagen SAXD peak (**Figure S2**), in a manner similar to our previous work [15]. Details are provided in **Supplementary Information**.

Matching to experimental data: Least-squares minimizations was carried out by simultaneously fitting the experimental E_f and E_m data to the model expressions (**Figure 5** and **Figure S6** in **Supplementary Information**). Each fitted experimental point (at a given strain rate) was weighted by the inverse of its squared standard deviation [60]. The weighted fitting process was performed in *Matlab* with the function *Nlinfit* [53] (**Table 1** and implementation in **Supplementary Information**). **Table 2** describes the choice of the input parameters for the model.

363 **2.9.2 Finite element simulations of fibrillar and lamellar reorientation**

1
2
364 To simulate the load-induced reorientation of fibrils toward the loading axis, an approximate method
365 was used, based on finite element simulations. The reorientation of a fibril embedded in an
366 extrafibrillar matrix was determined (**Figure 3B**), assuming isotropic material properties (**Table S2**),
367 by applying a uniform traction of 10 MPa to the top edge of the fibril and calculating angular
368 reorientation from the horizontal and longitudinal displacements. Details are provided in
369 **Supplementary Information.**

11
12
13
14
15
16
17
18
19
20
21
22
23
24
25
26
27
28
29
30
31
32
33
34
35
36
37
38
39
40
41
42
43
44
45
46
47
48
49
50
51
52
53
54
55
56
57
58
59
60
61
62
63
64
65

372 **Table 2: Elastic material properties of the basic components and their volume fractions in the**
 373 **Wild and GIOP models at low, medium and high strain rate values. Red: values extrapolated from**
 374 **referenced literature; Blue (with light blue background): values obtained from the fitting process;**
 375 **Black with dark grey background: values that were assumed. The k-factor is linked to the**
 376 **reinforcement of the collagen fibrils by the mineral platelets (Eqns. S2 and S6 in Supplementary**
 377 **Information).**

<i>Young's moduli</i>	GIOP bone (GPa)				Wild-type bone (GPa)	
E_c = Young's modulus of collagen	2.5 [36]				2.5 [36]	
E_m = Young's modulus of hydroxyapatite (mineral content)	100 [36]				100 [36]	
E_{EM} = Young's modulus of extrafibrillar matrix		$k = 1.58$	$k = 1.6$	$k = 1.7$		Extrafibrillar matrix
	low s.r.	163.8	107.6	53.0	low s.r.	3.5
	medium s.r.	160.8	105.7	52.3	medium s.r.	159.0
	high	160.1	105.3	52.1	high	370.0
<i>Poisson's ratios</i>						
ν_c = Poisson's ratio of collagen	0.3 [61]				0.3 [61]	
ν_m = Poisson's ratio of hydroxyapatite (mineral content)	0.28 [61]				0.28 [61]	
ν_{EM} = Poisson's ratio of extrafibrillar matrix	0.3 [61]				0.3	
<i>Volume fractions</i>						
ϕ_c = volume fraction of collagen	0.6				0.55	
ϕ_m = volume fraction of hydroxyapatite (mineral content)		$k = 1.58$	$k = 1.6$	$k = 1.7$	0.45 - $\phi_{EM} = 0.37$	
		0.37	0.34	0.27		
ϕ_{EM} = volume fraction of extrafibrillar matrix		$k = 1.58$	$k = 1.6$	$k = 1.7$	0.08 (from fitting)	
		0.03	0.06	0.13		

3 Experimental Results and Model Fitting

3.1 X-ray Microtomography

X-ray microtomography was performed to investigate 3D micromorphometry, microscale mineralization distribution and possible mineralization defects of femora from wild-type and GIOP mice. A series of 8-bit grey level slices were obtained from the 3D tomograms of samples. **Figure 2** showed representative 2D slices for both longitudinal and transverse cross sections of femora from wild-type and GIOP mice. The 2D slices of transverse cross sections of femora, as shown in **Figure 2A** and **C**, are selected from mid-shaft of mice femora as indicated by red dash lines in **Figure 2B** and **D**. Clear qualitative differences can be observed in the cortical microstructure of GIOP mice as compare with wild-type mice. Both of the transverse and longitudinal cross sections of femoral from GIOP mice showed a very large fraction of cavities with less mineralized bone tissue near the endosteal cortex, whereas no such cavities were found in the femoral mid-shaft of wild-type mice. The femoral cross section of GIOP mice showed a much thinner cortex compared to wild-type mice.

This is in agreement with backscattered electron (BSE) imaging results of the cross section of mice femoral mid-diaphysis (as also carried out in [15]), which showed 2D porosity coefficients of $1.68 \pm 0.26\%$ and $29.57 \pm 1.74\%$ for wild-type and GIOP bone, respectively.

Histograms of degree of mineralisation and the mean mineral concentration of middle shaft femoral bone from wild-type (N=5) and GIOP (N=5) mice were measured using X-ray microtomography. Representative distributions of mineral concentration were plotted for mid-shaft femora from wild-type and GIOP mice (**Figure 2E**). While not clearly visible at the lower-magnification whole-bone CT slices in **Figure 2A-D**, our prior work using backscattered electron microscopy on GIOP vs WT-femora (at similar age-points) showed that the mineralization of the endosteal region is clearly lower than the periosteal region in GIOP, while it is similar across regions in WT [33]. Since two distinct regions of interest: endosteal region surrounded by less mineralized halos, and periosteal region, were observed in GIOP mice (**Figure 2C, D**)[33], they were used separately for quantitative X-ray microtomography analysis (**Figure 2** inset **C1**). The weighted average mineral concentrations (denoted as the degree of mineralisation) measured as hydroxyapatite g/cm^3 were calculated from the frequency distribution of mineral concentration and plotted for different groups (**Figure 2E-F**). One-way ANOVA test indicated that the mean mineral concentration among three groups were significantly different. The weighted average mineral concentration in wild-type mice is significantly higher than that in GIOP periosteal ($p < 0.01$) and endosteal regions ($p < 0.001$), and it is also significantly higher ($p < 0.01$) in GIOP periosteal regions compared to GIOP endosteal regions

(Figure 2F). The broad distribution of mineral concentration with a fat tail toward low mineral concentration in GIOP endosteal region indicated a microscale heterogeneous mineralisation.

3.2 *In situ* tensile testing with synchrotron SAXD and WAXD

SAXD and WAXD patterns: Representative SAXD and WAXD patterns for femoral mid-shaft of wild-type mice aged 24 weeks are shown in Figure 1E and 1G, and 1D intensity profiles of the third-order collagen reflection and (002) mineral reflections in mice femur mid-diaphysis are shown in Figure 1F and 1H.

Effective fibril moduli: To compare the fibrillar-deformation in mice femur tested at different strain rates (Figure 5B and Figure 4A, D), data for samples at each strain rate were combined and plotted (tissue stress vs. nanoscale fibrillar strain) in the elastic deformation region (Figure 4A, D), and show differences in the slope (effective fibril modulus $E_f = d\sigma/d\epsilon_f$). Average effective fibril moduli from each group of samples were plotted as a function of strain rate in Figure 5B (pink bars). As strain rate increased from 0.0004 s^{-1} to 0.02 s^{-1} , we observe a significant increase in the effective fibril modulus increased from $13.6 \pm 3.0 \text{ S.D. GPa}$ to $65.6 \pm 11.4 \text{ S.D. GPa}$ ($p < 0.001$) in wild-type mice bone.

In contrast, the effective fibril modulus remains nearly constant in GIOP mice bone (blue bars). The effective fibril modulus in wild-type mice are significantly ($p < 0.001$) higher compared to GIOP mice at strain rates 0.01 and 0.02 s^{-1} , no significant differences in the effective fibril modulus between wild-type and GIOP mice was found at strain rate 0.0004 s^{-1} (Figure 4 and Table 3). Note that for the data plotted in Figure 5 B-D, the parameters E_f , E_m and rate of fibrillar reorientation are calculated per-sample and averaged within each strain-rate group, whilst the lines in Figure 4 are regressions through the pooled data points (tissue stress vs fibril strain, mineral strain or reorientation) from all samples at that strain-rate. This difference accounts for slight differences in the slopes between the Figures: for example, the averaged fibril moduli in GIOP is lowest at the highest strain rate (0.02 s^{-1} ; Figure 5B) while the slope of the regression line for GIOP-bone in the fibril moduli plot in Figure 4D is lowest for the intermediate strain rate 0.01 s^{-1} .

Effective mineral moduli: In a parallel manner, considering the mineral crystallite deformation, tissue stress versus mineral strain were grouped and plotted for three different strain rates (Figure 4B, E). Here, the effective mineral modulus ($E_m = d\sigma/d\epsilon_m$) in wild-type mice bone increased with strain rate and the increase was significant ($p = 0.026$) as seen in Figure 5C (dark blue bars). E_m increased from $44.2 \pm 7.3 \text{ S.D. GPa}$ to $97.5 \pm 28.3 \text{ S.D. GPa}$ as strain rate increased from 0.0004 s^{-1} to 0.02 s^{-1} in wild-type mice bone. In contrast, E_m remains nearly constant in GIOP mice bone (blue bars). The

444 effective mineral modulus in WT mice were significantly higher compared to GIOP mice at all strain
 445 rates (**Figure 4** and **Table 3**).

446 **Fibrillar reorientation**: Considering the fibrillar orientation with respect to the direction of loading,
 447 the azimuthal intensity distributions of the first-order collagen reflection from mice femur were used
 448 to determine the degree of fibrillar orientation (FWHM) at unstrained state and the change of FWHM
 449 during tensile loading. Wild-type mice bone shows that 1) the FWHM consistently narrows with
 450 increasing strain, but 2) the percentage-change reduces dramatically as the strain rate increases
 451 (**Figure 4C**). Averaged values of the rate of fibrillar reorientation were plotted as a function of strain
 452 rate in **Figure 5D**, and showed a significant ($p = 0.018$) reduction. In wild-type mice bone, the rate of
 453 fibrillar reorientation (-40.8 ± 23.2 S.D. $^{\circ}\%^{-1}$) at low strain rate (0.0004 s^{-1}) is significantly higher as
 454 compared to strain rates of 0.01 s^{-1} ($p = 0.034$) and 0.02 s^{-1} ($p = 0.025$).

455 In contrast, for GIOP bone there are no significant differences in reorientation rate with strain rates.
 456 The reorientation rate in GIOP mice bone at strain rate 0.0004 s^{-1} is significantly lower than that in
 457 wild-type bone, whereas no significant differences in reorientation rate was found between wild-type
 458 and GIOP mice bone at strain rate 0.01 s^{-1} and 0.02 s^{-1} (**Figure 4** and **Table 3**).

459 **Table 3: Effective fibril moduli, effective mineral moduli and fibrillar reorientation in WT- and**
 460 **GIOP-bone; p-values report differences between WT- and GIOP- in each group.**

	Strain rate (s^{-1})	Wild-type	GIOP	P-value
Effective fibril moduli (GPa)	0.004	13.60 ± 3.00	14.46 ± 2.66	0.876
	0.01	37.90 ± 9.90	13.02 ± 4.28	< 0.001
	0.02	65.60 ± 11.40	11.50 ± 3.58	< 0.001
Effective mineral moduli (GPa)	0.004	44.20 ± 7.29	17.90 ± 5.30	0.032
	0.01	70.50 ± 16.70	20.77 ± 1.42	< 0.001
	0.02	97.49 ± 28.38	26.66 ± 10.50	< 0.001
Reorientation rate (degree / %)	0.004	40.75 ± 23.22	2.18 ± 9.65	< 0.001
	0.01	4.90 ± 3.91	1.76 ± 5.63	0.703
	0.02	5.50 ± 4.94	1.24 ± 4.02	0.606

462 3.3 Model fitting to experimental E_f , E_m and reorientation:

463 An initial fitting process for the two models allowed the Young's moduli corresponding to the three
 464 analyzed strain rate values and the volume fraction of the extrafibrillar matrix (**Figure 5A**) to be
 465 calculated. **Figure 5A** shows the variation of the modulus of extrafibrillar matrix. In the wild-type

466 case the extrafibrillar matrix stiffens by over a factor of 100 – from 3.5 GPa at $\dot{\epsilon} = 0.0004 \text{ s}^{-1}$ (low
1
467 strain rate) to 370.0 GPa at $\dot{\epsilon} = 0.02 \text{ s}^{-1}$ (high strain rate). In the GIOP case, instead, depending on
3
468 the imposed k -factor and on the strain rate, values of the extrafibrillar Young's modulus can range
5
469 between 52.1 and 163.8 GPa (**Table 2**).

7
470 **Figure 5B** shows a comparison between the experimental and numerically computed effective fibril
9
471 modulus E_f . For the wild model, the results show agreement within the experimental error bars,
11
472 underestimation at medium and high strain rate values and overestimation at the low strain rate
13
473 ($\dot{\epsilon} = 0.02 \text{ s}^{-1}$). For the wild-type model a stiffening effect with an increasing strain rate – as seen in
15
474 experiment – was also found at the mineral level (**Figure 5C**). The effective mineral modulus, E_m , is
16
475 overestimated at high and medium strain rates and slightly underestimate at low strain rate.

18
476 For the GIOP bone, both the effective fibrillar and mineral moduli confirm the constant trend found
19
21
477 experimentally (**Figure 5B-C**) and show agreement with experimental values (average experimental
23
478 13.6 GPa vs 13.9 GPa). Indeed, the average experimental value of the effective fibril modulus at the
24
479 3 strain rates is 13.6 GPa while the corresponding modelling value is 13.9 GPa. Corresponding
26
480 values for the effective mineral modulus are respectively 22.8 GPa and 21.8 GPa.

28
29
481 **Figure 5D** shows that for lamellar-level fibrillar reorientation – calculated via change of $\Delta FWHM$
31
482 normalised by the fibril strain – the wild-type model reproduces the trend to reduced reorientation
32
483 with increased stress. For the GIOP model a reduction of the k -factor (**Equation S6**) lead to a
34
484 reduction of fibrillar reorientation (**Figure 5D**). Our parametric analysis shows that the reorientation
36
485 calculated via FE simulations matches the experimental reorientation (modelling values within the
38
486 experimental error bars) for 3 strain rates assuming $k = 1.58$.

4 Discussion

Strain-rate dependent tensile tests were performed on small femoral samples of wild-type and steroid-induced osteoporotic (GIOP) mice. Our main findings can be summarized as follows:

- Under tensile testing with increasing strain rate, the fibrillar-level deformation of GIOP bone exhibits a contrasting behaviour to wild-type (WT; normal) murine bone – specifically, while WT-bone shows a significant increase in effective fibril- and mineral-moduli, this effect is absent in GIOP bone
- On increasing strain-rate, WT-bone shows a significant reduction of extent of fibrillar reorientation toward the loading axis; in contrast, GIOP bone shows no change in reorientation with strain-rate.
- By comparing the volume-average SAXS- and WAXD-measures of fibril- and mineral-strain to the model predictions of a fibril/fibril-array model of bone matrix mechanics, the strain-rate dependent effects in WT-bone are explained via an increased extrafibrillar matrix stiffening.
- In contrast, for GIOP-bone, the experimental results can be matched to model predictions if the reinforcement between mineral- and collagen (via the k -factor; **Table 2**) at the nanoscale is taken higher for GIOP compared to WT, and no extrafibrillar matrix stiffening occurs in GIOP-bone.

The novelty of the current study is primarily in obtaining experimental data characterising how the strain-rate dependence of fibrillar deformation mechanics in osteoporotic bone differ from normal cortical bone, and as a secondary goal, to explore the underlying structural mechanism by fitting a multilevel model to the data. Prior work, by our group as well as others [14, 15, 33, 42] have analysed alterations in fibrillar mechanics in metabolic bone disorders like rickets, GIOP, and ageing, but these have not studied strain-rate dependence in such pathological conditions. Because bone is used in a dynamic mechanical environment, understanding how the structural response of the bone matrix at the fibrillar level alters with increasing strain rate is of direct interest. From a materials-standpoint, for example, our observation that the fibril strain gradient (from E_f) is unchanged at different strain rates in GIOP-bone, but decreases in WT-bone (**Figure 4**), provides insight into the altered biomechanical reinforcing efficiency of the collagen fibrils. Further, while the current work does not directly deal with fracture, prior work by other groups has shown that strain-rate influences work of fracture, with reduction of work of fracture and transition to unstable crack growth with increasing strain rate [62, 63], as well as increase of elastic moduli and yield strength [64]. Indeed, if

520 fibrils in osteoporotic GIOP bone show no change with increasing strain rate, while an effective
521 “stiffening” is seen via the increased fibril modulus in normal (WT) bone, this may lead to a lower
522 mechanical competence in GIOP at higher strain-rates compared to WT. When compared with the
523 wild-type bone, the relationship between strain rate and increasing modulus breaks down for GIOP,
524 indicating the mineral-collagen composite in GIOP failed to adequately stiffen with increasing strain
525 rate, which is likely the cause of the lowered mechanical competence. While the lower maximal
526 fibril strain in WT relative to GIOP sounds counterintuitive when one associates disease with
527 lowered strength and brittleness, we note that a) the total tissue strain is a complex sum of the fibril,
528 interfibrillar, and interlamellar level strains and b) the maximal elastic stress level in GIOP is lower
529 than WT. Therefore, the expected weak (lower strength) behavior in GIOP is present, whilst the
530 lower maximal fibril strain in WT- does not exclude that the maximal strain at macroscopic failure
531 will still be lower in GIOP than WT (possibly due to tissue-level defects and pores). We note,
532 however, an underlying assumption in our work is that the mouse model of endogenous
533 glucocorticoid production (Cushing’s syndrome) is a valid and relevant model for (exogenous)
534 human GIOP [40]. As mouse models do not exhibit secondary remodelling, the bone structure at the
535 tissue level will be different from human GIOP.

536 The strain-rate dependence of the mechanical properties of bone have been studied at the
537 macroscopic level before [58, 64-66], using phenomenological viscoelastic/viscoplastic models or
538 relations such as the Ramberg-Osgood equation used earlier. The nature of the structural mechanisms
539 in time-dependent mechanical loading is less studied. High strain-rate *in situ* SAXD measurements
540 on human bone found a strain-rate induced stiffening of the fibril ductility associated with a loss in
541 toughness in bone matrix [38], and compressive creep studies found the strain on both mineral and
542 collagen phases in bone increase linearly with time, proposed as a load-shedding from collagen to
543 mineral [67]. Stress-relaxation was observed to be more rapid in mineral than in collagen [68].
544 Molecular dynamics studies (e.g. [69]) have highlighted the role of rapidly breaking and reforming
545 hydrogen bonds during deformation. Nevertheless, structural-mechanisms enabling viscoelasticity in
546 the bone matrix are not clearly known, and the experimental data on the variation of the time-
547 dependent behaviour in osteoporosis presented here may help toward that eventual goal. It is noted
548 that the exposure of the samples to X-rays is consistent across three different strain-rates. By closing
549 the shutter between acquisitions, and keeping acquisition time constant at 0.1s per point, the total X-
550 ray dose is proportional to the number of SAXS patterns per tensile test. Figure S5 (Supplementary
551 Information) shows that the number of patterns is of the same order of magnitude across strain-rates.
552 Therefore, it is not likely that the high-strain rate tests are being exposed to much higher X-ray

dosages compared to the low- and medium strain-rates, which would cause damage to the collagen matrix [44].

The experimental values for maximal fibril strain (**Figure 5A**) at low strain rates (~0.4-0.6%) are consistent with our prior quasi-static results on both murine [15, 33, 42] and bovine bone [37], and in the same range as those observed by others on human bone [14]. In WT-bone, the maximal fibril strain reduces consistently from ~0.6% at the lowest strain rate (0.0004 s^{-1}) to ~0.1% at the highest strain-rates (0.02 s^{-1}). However, a similar trend is not visible for GIOP; for intermediate strain rates (0.01 s^{-1}) in GIOP-osteoporotic bone – in **Figure 4D**, maximum fibril strain can reach ~0.6-0.8% compared to the ~0.4% values for the lowest strain-rate, while for the highest strain rate the maximum fibril strain is again ~0.4%. Since maximum strains are linked to strength and failure of the entire bone, microstructural differences between GIOP- and wild-type bone (**Figure 2**) may be relevant in explaining this behaviour, which is beyond the scope of the nano/microscale model presented and discussed below.

Fibrillar reorientation, as well, shows some notable differences between GIOP and WT. Here, it is important to note certain experimental limitations. As SAXD and WAXD provide volume averaged measures of fibrillar/mineral structure through the thickness of cortical bone specimens used in these tests, effects *below* and *above* the scale of the fibril cannot be excluded. Consequently, if the sample volume contained microscopically misaligned lamellae, these could undergo inter-lamellar reorientation, rather than the reorientation occurring at the fibril/interfibrillar matrix alone (this corresponds to phenomena above the scale of the fibril). Likewise, it is known that tropocollagen molecules inside microfibrils are arranged in a tilted geometry [70] and intrafibrillar rearrangement may also contribute, rather than fibrils rotating in a rigid-body manner. **However, we note that the numerical value of the tilt inside microfibrils is small (~4° in Figures 2-3 in [70]) (noting the factor of 5 compression in the c-axis direction specified by the authors). This value is much smaller (Figure 5D) compared to the ~50° (FWHM change)/% strain reorientation seen for the lowest strain rate. Therefore, load-induced intrafibrillar rotation of the molecules, to remove the tilt, would be insufficient to explain the magnitude of the observed reduction in FWHM. To be able to overcome the averaging issue inherent in our experimental configuration, possible future routes may involve 6D SAXS tensor tomography [71], if challenges in data processing and potential radiation damage are overcome. Such methods can provide spatially-resolved 3D maps of the fibrillar nanostructure across the tissue, although time-resolved studies at the strain-rates proposed here (and above) will still be challenging. Subfibrillar-level deformation may be analysed by the covariation of changes in the angular intensities of the WAXD and SAXS patterns (which will provide information**

586 on how the mineral particles are reorienting relative to the fibrils), or possibly by contrast-variation
587 neutron diffraction to resolve the changes in tropocollagen ordering.

588 While the empirical differences between the strain-rate dependencies in the GIOP- and WT-
589 nanoscale parameters (E_f and E_m) is clear from **Figures 4-5**, these numbers (averaged across
590 scattering volume) by themselves do not provide a full structural explanation. From our earlier
591 studies on GIOP-bone [15, 33], the orientation distribution is wider in GIOP than WT. These facts
592 imply that earlier simpler models, such as our prior work on antler [36], which modelled the uniaxial
593 fibrils alone (oriented along the loading axis), are likely insufficient to explain the data. As a first
594 step in this direction, we used a two-level multiscale model of bone nano- and microstructure to
595 provide some insights into possible reasons for these changes. At the fibrillar level, the model is
596 similar to prior staggered models of mineral-collagen interactions put forward [11, 36, 41, 55-57, 61,
597 72], although the inclusion of the mechanics of the extrafibrillar matrix is an advance on our prior
598 modelling [36]. At the fibril-array level (microscale), bone is known to have a lamellar structure
599 although the precise details of the orientation (originally proposed as plywood or rotated plywood
600 [13, 73]) are still not fully clear, with recent revisions to the orientation scheme proposed [12] to
601 incorporate a fraction (10%) of disordered fibrils. The plywood scheme used in the original paper [13]
602 is used here (also for consistency with prior modelling work [61]), but inclusion of more complex
603 structures to model the experimental results is possible in the future. Further, the microstructure of
604 rat and mice bone is different from human bone, which has extensive secondary remodelling and
605 well developed secondary osteons, and these differences are not accounted for in the model. In
606 addition, spatial variations in bone matrix parameters at larger length scales than the nano- and
607 micro- (such as across cross-sections of cortical bone reported in rat bone [74]) are beyond the scope
608 of the model, even though clear variations between endosteal and periosteal regions (**Figure 2**) are
609 visible. Parameter estimates from the model and their structural interpretation below need therefore
610 to be considered as estimates rather than definitive values.

611 From optimizing the parameters for model predictions to agree with experimental values of
612 effective fibril- and mineral-moduli, it is observed that in normal WT cortical bone the stiffening of
613 the extrafibrillar matrix with increasing strain-rate can lead to the increased fibril (and mineral)
614 modulus seen experimentally (**Figure 5**). Increased stress borne by the extrafibrillar matrix reduces
615 the strain on the fibrils, which therefore increases the effective fibril modulus, which is a ratio of
616 macroscopic stress to fibril strain. A similar process occurs for effective mineral moduli. The
617 extrafibrillar space in bone contains extrafibrillar mineral and non-collagenous proteins [75, 76], and
618 we can speculate that such a phase of mineral interlinked with protein may exhibit strain-stiffening

619 behaviour with increasing strain-rate, being dominated by the moduli of the noncollageneous
620 proteins (< 1 GPa) at low strain rates and by the modulus of the mineral at larger strain rates.
621 However, we obtain unrealistically high values for the modulus of the extrafibrillar matrix (370 GPa)
622 at the highest strain rate, well above the 100-110 GPa characteristic of hydroxyapatite mineral [36].
623 Possibly, these values arise from the extrafibrillar volume fraction or type of orientation distribution
624 used here, and parametric-variation studies may be useful in future in this regard.

625 In contrast, the experimental data for the GIOP-bone can be fit to the model with essentially
626 constant extrafibrillar matrix moduli (**Table 2**) but with a considerably lowered *k*-factor. The
627 physical meaning of this difference compared to WT bone is not fully clear. The *k*-factor is inversely
628 linked to the reinforcing efficiency of the mineral platelets inside the collagen fibril [11, 36], and
629 arises due to the load-transfer from the collagen matrix to the mineral platelet. Note that the effect of
630 the more random fibril orientation in GIOP [15, 33] has already been included via the wider FWHM
631 from $I(\chi)$. As the *k*-factor depends on the effectiveness with which loads are transferred to the
632 mineral from the collagen, the differing *k*-factor in GIOP compared to WT suggests that possibly the
633 orientation and/or interactions of intrafibrillar mineral with collagen may differ. However, this still
634 does not explain why we do not obtain a similar strain-rate dependent stiffening as seen in WT-bone.
635 We can speculate that these open questions are linked to limitations of our model. As the fibril
636 orientation distribution is not precisely the multilayer lamellar structure described initially [13] but
637 includes random fibril orientations [12], and the further differences in lamellar structure in GIOP
638 have not yet been determined, it is likely that further alterations or refinements to the structural
639 model will be needed, even though the experimental differences between GIOP- and WT-bone
640 fibrillar strain-rate dependencies are not in question.

641 A limitation of the current work is that we did not report results of varying the collagen- and
642 mineral-moduli in the model, both of which may change in disease due to substitution of ions and
643 change in covalent crosslinking [14, 77]. In this regard, we have observed (data not shown) that
644 variation of collagen moduli cannot explain the increase in effective mineral moduli (**Figure 5C**)
645 with strain rate. Regarding the mineral phase, our previous study [15] showed that, compared to WT
646 bone, the mineral platelet is slightly shorter (in length, along the c-axis) and the intra-platelet lattice
647 spacing is slightly higher in GIOP bone, but the mechanical implications of these crystallographic
648 changes is not clear to us at this point. Perhaps, future *ab initio* molecular dynamics simulations of
649 the change in mineral crystallite structure [78], linked to simulated mechanical testing at these small
650 scales, could shed light on this question.

651 In summary, we have analysed for the first time the fibrillar- and mineral-level strain changes
652 in steroid-induced osteoporotic and normal murine bone with increasing strain-rate, and have found
653 both a) clear changes with strain-rate for normal bone and b) a near constant-response across strain-
654 rates for osteoporotic bone. Modelling the bone matrix as arrays of mineralized fibrils with
655 intervening matrix, our results suggest alterations in extrafibrillar matrix stiffness and mineral-
656 collagen reinforcement factors may be the underlying factors. Our results provide insight into the
657 time-dependent nature of fibrillar mechanics in both normal and osteoporotic bone, and may be
658 relevant in understanding the structural origins (in terms of bone quality) of the lower mechanical
659 competence in osteoporosis.

660 **Acknowledgments**

661 This work was supported by Diamond Light Source (Harwell, UK), Queen Mary University of
662 London (grant no. SEML1B4R), the Medical Research Council UK (grant no. G0600702) and the
663 National Science and Technology Major Project (2017-V I -0020-0093). L.X. is supported by the
664 China Scholarship Council (CSC). NMP is supported by the European Commission with the
665 Graphene Flagship Core 2 n. 785219 (WP14 “Composites”) and FET Proactive “Neurofibres” n.
666 732344 as well as by the MIUR with the “Departments of Excellence” grant L. 232/2016, ARS01-
667 01384-PROSCAN Grant and the PRIN-20177TTP3S. We thank Diamond Light Source (Harwell,
668 UK) for the award of synchrotron beamtime to carry out the *in situ* SAXD/WAXD experiments
669 (SM9893, SM11806, and SM12483). HSG acknowledges support from BBSRC (BB/R003610/1)
670 and from UKRI (MR/R025673/1).

673

Figures:

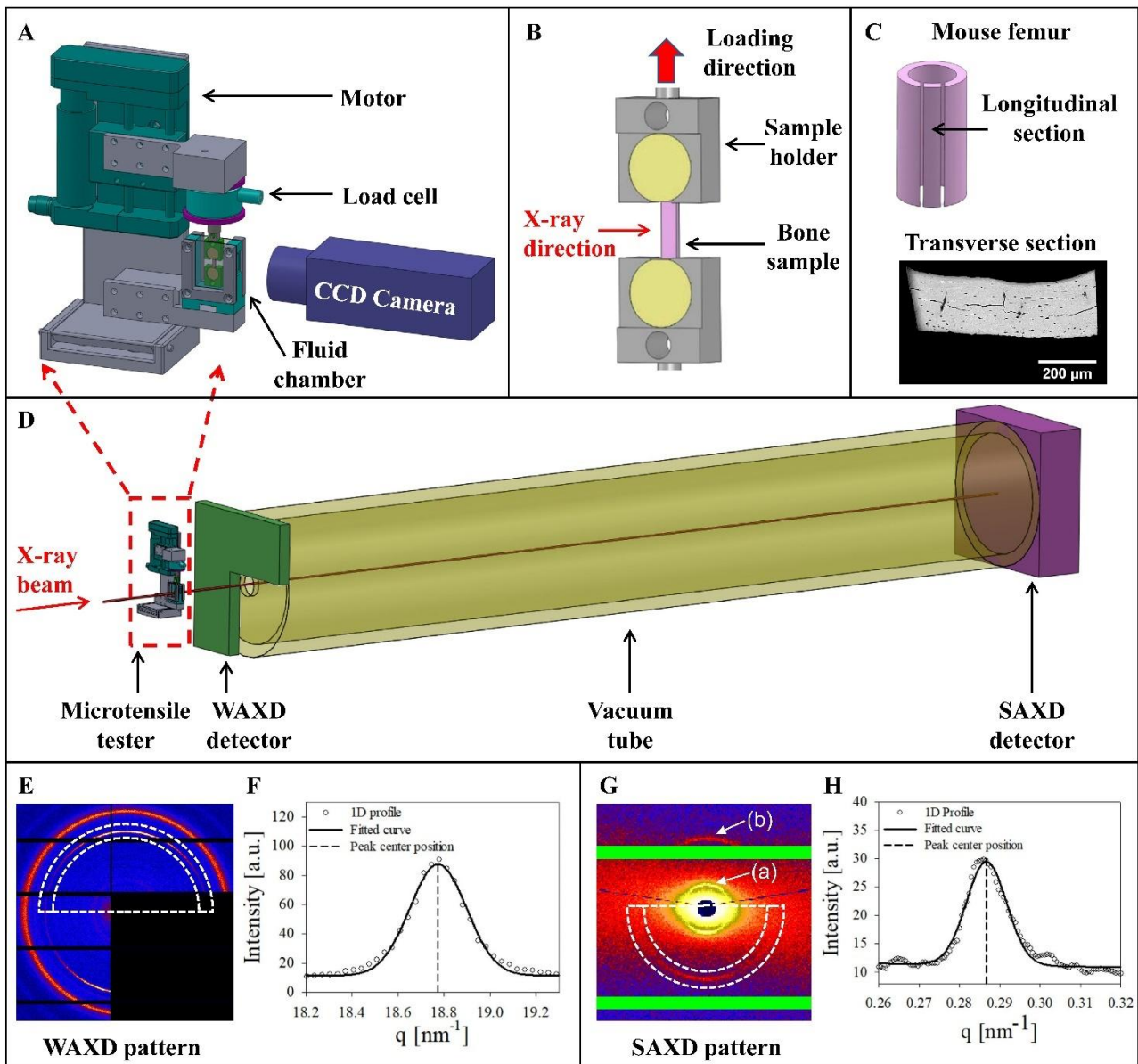


Figure 1: In situ nanomechanics with simultaneous synchrotron SAXD and WAXD. (A) Customized tensile tester with bone sample mounted in a fluid chamber. (B) Magnified view of sample and tensile grips in fluid chamber, with tensile strain along the vertical direction. (C) Upper: Schematic of mouse femur, with tensile test specimen sectioned along the long axis of femur; lower: backscattered electron image of transverse section of specimen. (D) Experimental configuration: Tensile tester with specimen mounted along the X-ray beam path in transmission geometry; an L-shape WAXD detector, vacuum tube and SAXD detector were positioned along the X-ray beam path. (E) 2D WAXD pattern from bone apatite with predominant c-axis orientation vertical. Dotted lines denote the 180° region for azimuthal averaging of intensity around the (002) peak of apatite. (F) Azimuthally averaged radial intensity profile $I(q)$ for the pattern in E. (G) 2D SAXD pattern from collagen fibrils in bone with predominant fibril orientation vertical. Dotted lines denote the 180° region over which the collagen reflection is averaged azimuthally; (a) the first-order and (b) the third-order collagen reflection. (H) Azimuthally averaged radial intensity profile $I(q)$ for the pattern

688 *in G. For F and H, black solid line: peak fit with a Gaussian function plus a linear baseline; black*
689 *dashed line: peak centre position.*

690

1
2
3
4
5
6
7
8
9
10
11
12
13
14
15
16
17
18
19
20
21
22
23
24
25
26
27
28
29
30
31
32
33
34
35
36
37
38
39
40
41
42
43
44
45
46
47
48
49
50
51
52
53
54
55
56
57
58
59
60
61
62
63
64
65

691
1
2
3
4
5
6
7
8
9
10
11
12
13
14
15
16
17
18
19
20
21
22
23
24
25
26
27
28
29
30
31
32
33
34
692
36
693
694
39
695
42
696
43
697
44
698
45
699
46
700
47
701
48
702
50
51
703
52
53
54
55
56
57
58
59
60
61
62
63
64
65

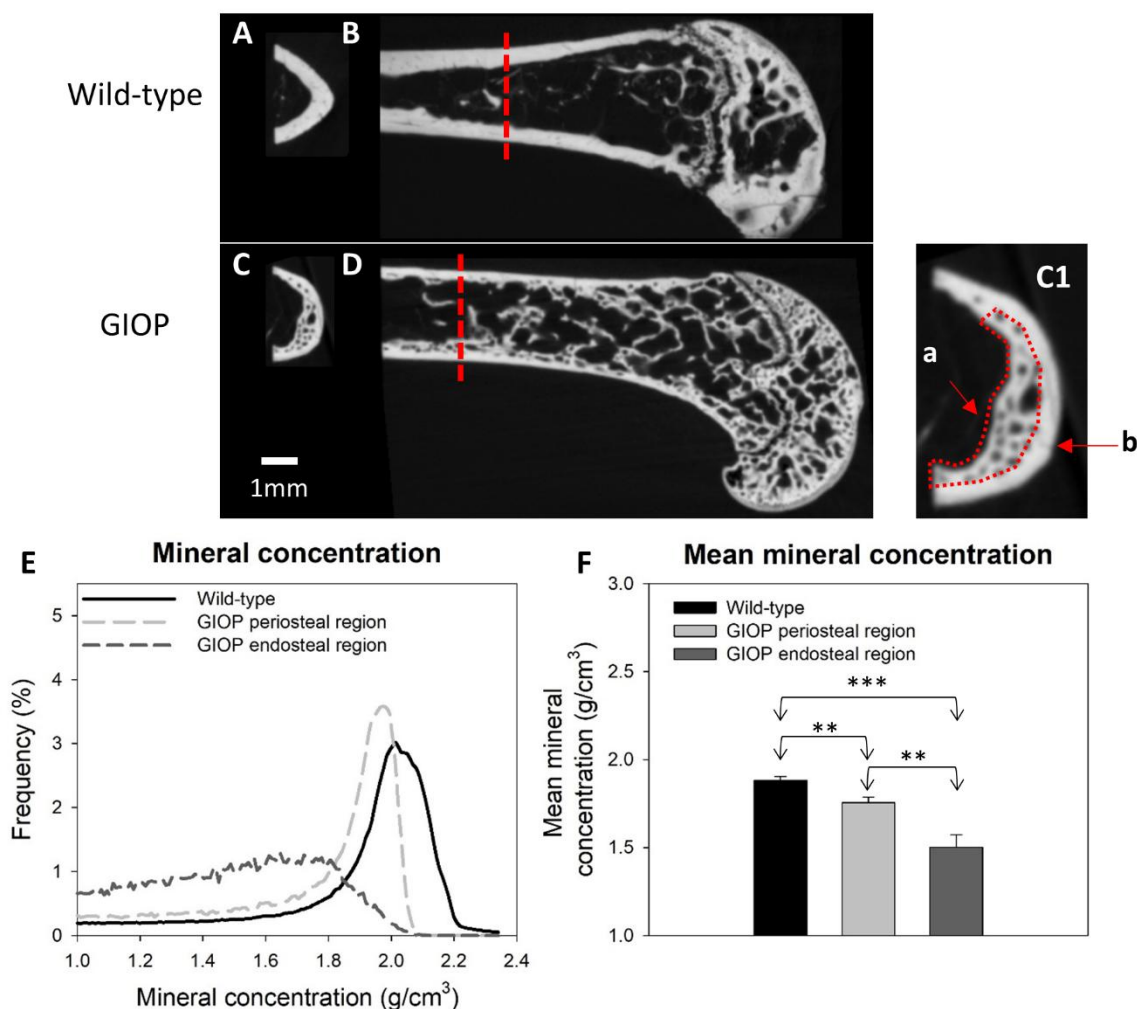


Figure 2: X-ray microtomography and degree of mineralisation. Representative 2D slices from X-ray microtomography measurement for both transverse (A, C) and longitudinal (B, D) cross sections of femora from wild-type and GIOP mice. Red dash line indicated location where the 2D slice of transverse cross section was taken. C1: Inset on right shows an example 2D transverse slice, with (a) indicating the endosteal region and (b) the periosteal region. (E) Representative histograms of degree of mineralisation were plotted for wild-type (black), GIOP periosteal regions (light gray) and GIOP endosteal regions (dark gray). (F) Bar chart of the mean mineral concentration for wild-type cortex, GIOP periosteal regions and GIOP endosteal regions. Error bars shown are standard deviations. Statistical significances were denoted on the figures (*p < 0.05, **p < 0.01, ***p < 0.001, ns: not significant).

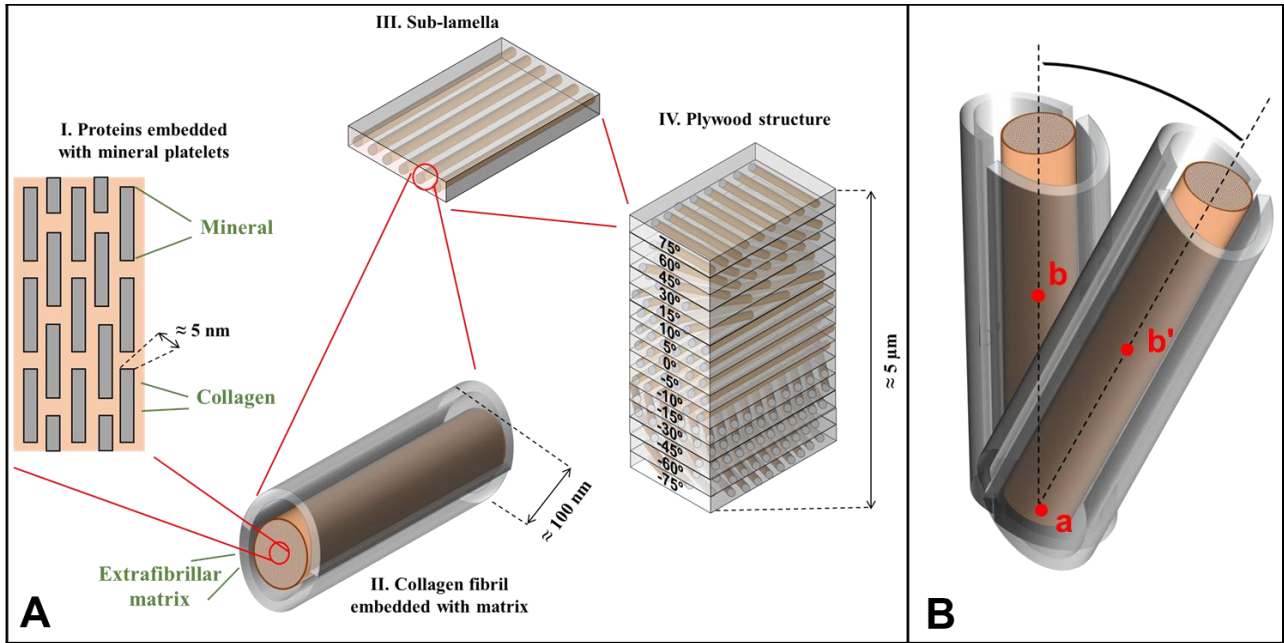
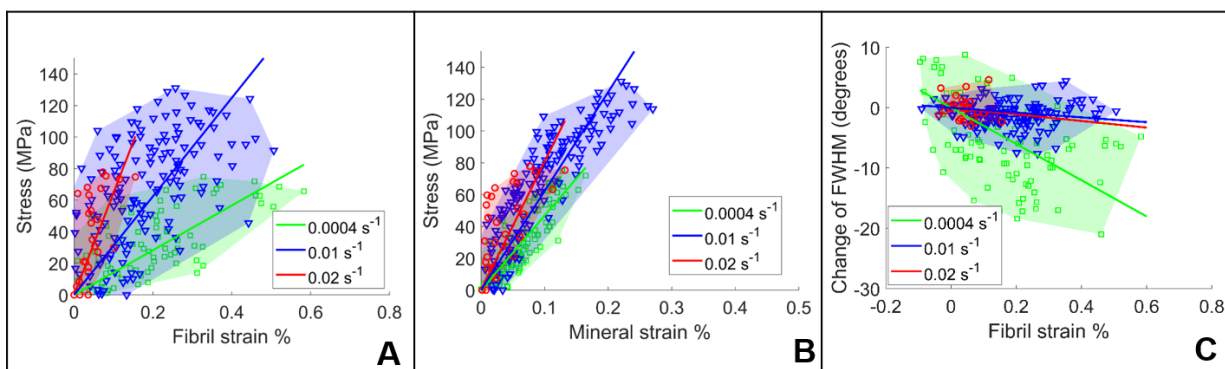


Figure 3: Schematic of the hierarchical structure of bone assumed for the modelling approach. A) I. At the lowest hierarchical scale, a staggered arrangement of hydroxyapatite mineral platelets and collagen [41] (left side of the figure) was considered. The material components are collagen, hydroxyapatite mineral and extrafibrillar matrix (which together form level II). A bunch of parallel collagen fibrils surrounded by an extrafibrillar matrix, forming a sublamella (III). A set of sublamellae, each with the longitudinal axis of fibrils pointing toward a specific direction, forms (IV) a plywood (or Bouligand [79]) system. For both modelling approaches the scheme in [13] with an angular distribution of sub-lamellae of the type: 0° , $\pm 5^\circ$, $\pm 10^\circ$, $\pm 15^\circ$, $\pm 30^\circ$, $\pm 45^\circ$, $\pm 60^\circ$, $\pm 75^\circ$, (0° direction is along the applied loads). B) Schematic for reorientation in the model.

Wild-type



GIOP

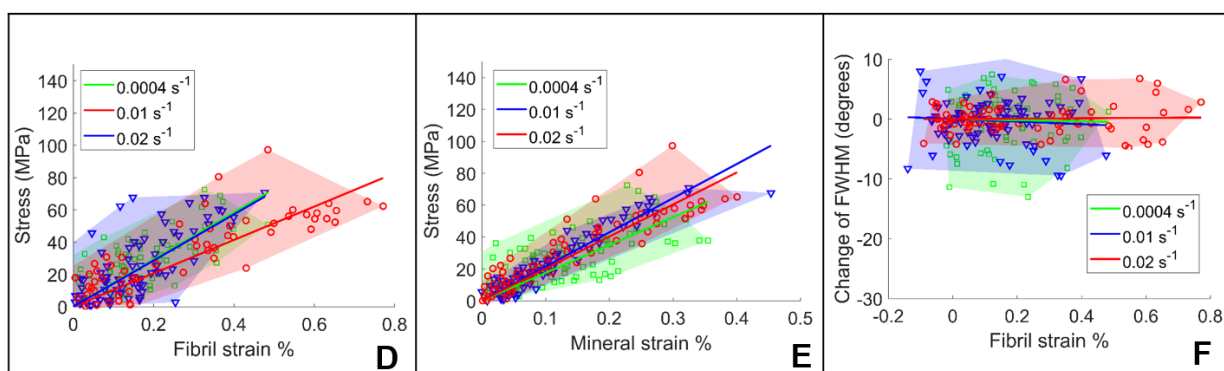


Figure 4: Fibril strain, mineral strain and change of FWHM from in situ synchrotron SAXD and WAXD: Symbol code: Low strain rate (0.0004 s^{-1} , green squares), medium strain rate (0.01 s^{-1} , blue triangles) and high strain rate (0.02 s^{-1} , red circles). (A, D) Applied tissue stress vs average fibril strain. (B, E) Applied tissue stress vs average mineral strain. (C, F) Change of the FWHM of a Gaussian profile vs average fibril strain (see also text and **Table 1** for parameter definitions). The symbols are experimental data points (pooled across samples for each strain rate) while the straight lines are linear regression lines for each group of data (regressions through pooled data points at a given strain-rate). The shadowed area in the six plots is a convex hull of the experimental data representing the region that numerical results are expected to intersect.

1
2
3
4
5
6
7
8
9
10
11
12
13
14
15
16
17
18
19
20
21
22
23
24
25
26
27
28
29
30
31
32
33
34
35
36
37
38
39
40
41
42
43
44
45
46
47
48
49
50
51
52
53
54
55
56
57
58
59
60
61
62
63
64
65

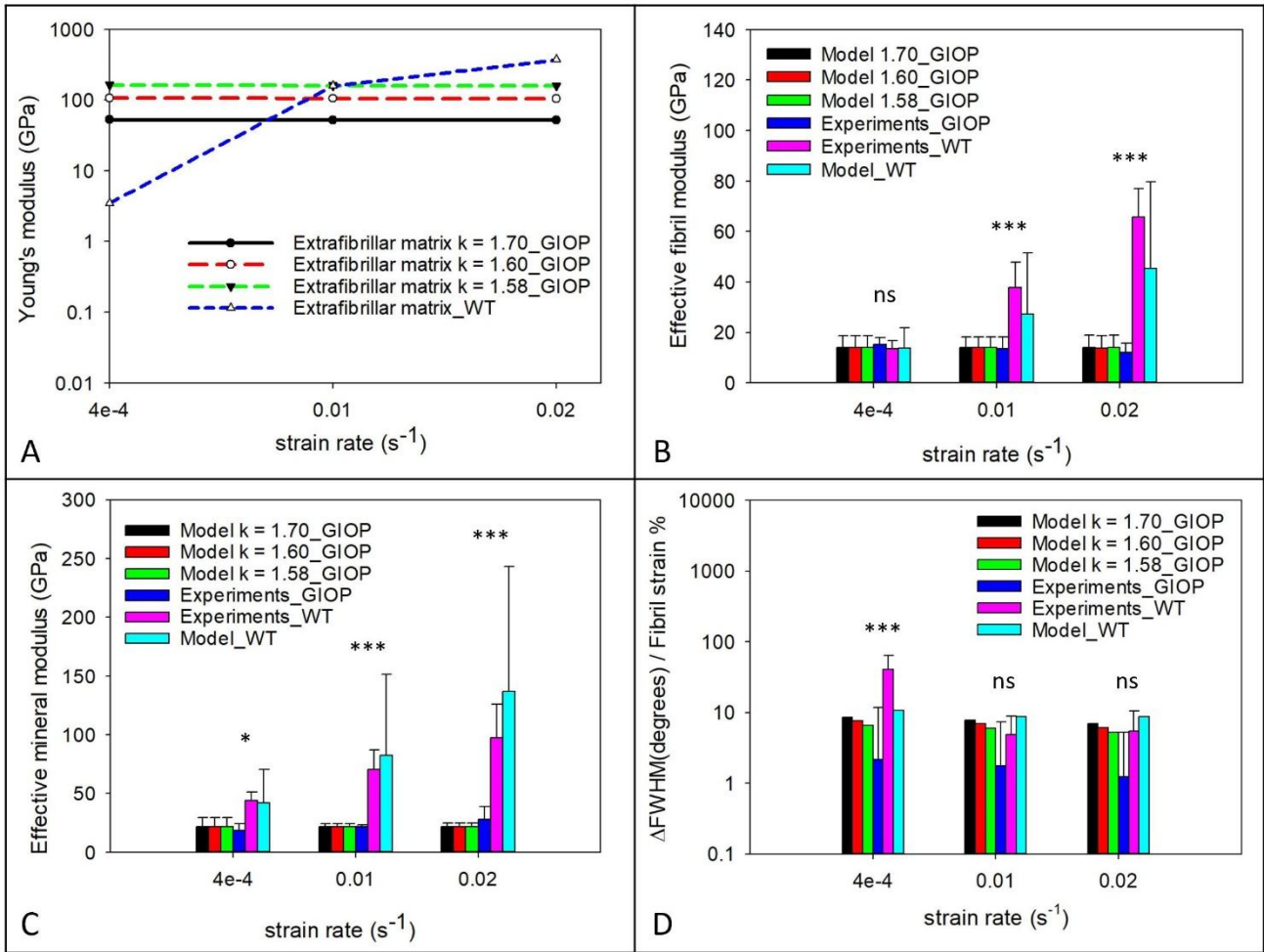


Figure 5: Nanoscale structural parameters of bone mineral and fibrils from experiments and modelling: (A) Young's modulus of collagen and extrafibrillar matrix at different strain rates from simulation results (in log scale). (B) Effective fibril modulus, (C) effective mineral modulus and (D) reorientation rate (in log scale) are plotted as a function of strain-rate. Error bars shown are standard deviations for experimental data while are 95% confidence interval from the fitting process. One-way ANOVA tests were performed to test for statistical differences in the experimental results of the effective fibril modulus, the effective mineral modulus and the fibrillar reorientation rate between samples tested at different strain-rates. Statistical significance is denoted (* $p < 0.05$, ** $p < 0.01$, *** $p < 0.001$, ns: not significant).

736 **References**

1
737 **Uncategorized References**

3
738 [1] J.A. Kanis, Diagnosis of osteoporosis and assessment of fracture risk, *The Lancet* 359(9321) (2002) 1929-
739 1936.

740 [2] E. Seeman, P.D. Delmas, Bone quality--the material and structural basis of bone strength and fragility,
741 *The New England journal of medicine* 354(21) (2006) 2250-61.

742 [3] A. Carriero, E.A. Zimmermann, A. Paluszny, S.Y. Tang, H. Bale, B. Busse, T. Alliston, G. Kazakia, R.O. Ritchie,
743 S.J. Shefelbine, How Tough Is Brittle Bone? Investigating Osteogenesis Imperfecta in Mouse Bone, *J Bone*
744 *Miner Res* 29(6) (2014) 1392-1401.

745 [4] J.D. Currey, The structure and mechanics of bone, *Journal of Materials Science* 47(1) (2012) 41-54.

746 [5] J. Currey, *Bones: Structure and Mechanics*, Princeton University Press 2002.

747 [6] J.D. Currey, Mechanical properties of vertebrate hard tissues, *Proceedings of the Institution of*
748 *Mechanical Engineers. Part H - Journal of Engineering in Medicine* 212(H6) (1998) 399-411.

749 [7] J.D. Currey, Effects of Strain Rate, Reconstruction and Mineral Content on Some Mechanical-Properties of
750 Bovine Bone, *Journal of Biomechanics* 8(1) (1975) 81-86.

751 [8] J.D. Currey, Role of collagen and other organics in the mechanical properties of bone, *Osteoporosis Int* 14
752 (2003) S29-S36.

753 [9] P. Zioupos, J.D. Currey, A.J. Hamer, The role of collagen in the declining mechanical properties of aging
754 human cortical bone, *Journal of Biomedical Materials Research* 45(2) (1999) 108-116.

755 [10] S. Weiner, H.D. Wagner, The material bone: Structure mechanical function relations, *Annual Review of*
756 *Materials Science* 28 (1998) 271-298.

757 [11] P. Fratzl, R. Weinkamer, Nature's hierarchical materials, *Progress in Materials Science* 52(8) (2007)
758 1263-1334.

759 [12] N. Reznikov, R. Shahar, S. Weiner, Bone hierarchical structure in three dimensions, *Acta Biomater* 10(9)
760 (2014) 3815-3826.

761 [13] S. Weiner, W. Traub, H.D. Wagner, Lamellar bone: structure-function relations, *Journal of structural*
762 *biology* 126(3) (1999) 241-255.

763 [14] E.A. Zimmermann, E. Schaible, H. Bale, H.D. Barth, S.Y. Tang, P. Reichert, B. Busse, T. Alliston, J.W. Ager,
764 R.O. Ritchie, Age-related changes in the plasticity and toughness of human cortical bone at multiple length
765 scales, *Proceedings of the National Academy of Sciences* 108(35) (2011) 14416-14421.

766 [15] L. Xi, P. De Falco, E. Barbieri, A. Karunaratne, L. Bentley, C.T. Esapa, N.J. Terrill, S.D.M. Brown, R.D. Cox,
767 G.R. Davis, N.M. Pugno, R.V. Thakker, H.S. Gupta, Bone matrix development in steroid-induced osteoporosis
768 is associated with a consistently reduced fibrillar stiffness linked to altered bone mineral quality, *Acta*
769 *Biomater* 76 (2018) 295-307.

770 [16] P.J. Thurner, C.G. Chen, S. Ionova-Martin, L. Sun, A. Harman, A. Porter, J.W. Ager, 3rd, R.O. Ritchie, T.
771 Alliston, Osteopontin deficiency increases bone fragility but preserves bone mass, *Bone* 46(6) (2010) 1564-73.

772 [17] T.P. Van Staa, R.F. Laan, I.P. Barton, S. Cohen, D.M. Reid, C. Cooper, Bone density threshold and other
773 predictors of vertebral fracture in patients receiving oral glucocorticoid therapy, *Arthritis and rheumatism*
774 48(11) (2003) 3224-9.

775 [18] J. Compston, Management of glucocorticoid-induced osteoporosis, *Nature Reviews Rheumatology* 6(2)
776 (2010) 82-88.

777 [19] F. Mirza, E. Canalis, Secondary osteoporosis: Pathophysiology and management, *European Journal of*
778 *Endocrinology* 173(3) (2015) R131-R151.

779 [20] R. Rizzoli, E. Biver, Glucocorticoid-induced osteoporosis: Who to treat with what agent?, *Nature Reviews*
780 *Rheumatology* 11(2) (2015) 98-109.

781 [21] A.L. Boskey, E. DiCarlo, E. Paschalis, P. West, R. Mendelsohn, Comparison of mineral quality and quantity
782 in iliac crest biopsies from high- and low-turnover osteoporosis: an FT-IR microspectroscopic investigation,
783 *Osteoporosis Int* 16(12) (2005) 2031-2038.

- 784 [22] W.J. Landis, An overview of vertebrate mineralization with emphasis on collagen-mineral interaction,
785 Gravitational and space biology bulletin : publication of the American Society for Gravitational and Space
786 Biology 12(2) (1999) 15-26.
- 787 [23] E. Canalis, G. Mazziotti, A. Giustina, J.P. Bilezikian, Glucocorticoid-induced osteoporosis:
788 pathophysiology and therapy, Osteoporosis Int 18(10) (2007) 1319-1328.
- 789 [24] R.C. Pereira, A.M. Delany, E. Canalis, Effects of cortisol and bone morphogenetic protein-2 on stromal
790 cell differentiation: correlation with CCAAT-enhancer binding protein expression, Bone 30(5) (2002) 685-91.
- 791 [25] V. Krishnan, H.U. Bryant, O.A. MacDougald, Regulation of bone mass by Wnt signaling, Journal of Clinical
792 Investigation 116(5) (2006) 1202-1209.
- 793 [26] E. Canalis, Wnt signalling in osteoporosis: mechanisms and novel therapeutic approaches, Nature
794 reviews. Endocrinology 9(10) (2013) 575-83.
- 795 [27] D. Jia, C.A. O'Brien, S.A. Stewart, S.C. Manolagas, R.S. Weinstein, Glucocorticoids act directly on
796 osteoclasts to increase their life span and reduce bone density, Endocrinology 147(12) (2006) 5592-5599.
- 797 [28] H.J. Kim, H.B. Zhao, H. Kitaura, S. Bhattacharyya, J.A. Brewer, L.J. Muglia, F.P. Ross, S.L. Teitelbaum,
798 Glucocorticoids suppress bone formation via the osteoclast, Journal of Clinical Investigation 116(8) (2006)
799 2152-2160.
- 800 [29] P. Orcel, Updated recommendations on the management of glucocorticoid-induced osteoporosis, Joint
801 Bone Spine 81(6) (2014) 465-468.
- 802 [30] K. Hayashi, M. Yamamoto, Y. Murakawa, M. Yamauchi, H. Kaji, T. Yamaguchi, T. Sugimoto, Bone fragility
803 in male glucocorticoid-induced osteoporosis is not defined by bone mineral density, Osteoporosis Int 20(11)
804 (2009) 1889-1894.
- 805 [31] N.E. Lane, W. Yao, M. Balooch, R.K. Nalla, G. Balooch, S. Habelitz, J.H. Kinney, L.F. Bonewald,
806 Glucocorticoid-treated mice have localized changes in trabecular bone material properties and osteocyte
807 lacunar size that are not observed in placebo-treated or estrogen-deficient mice, J Bone Miner Res 21(3)
808 (2006) 466-476.
- 809 [32] R.S. Weinstein, D. Jia, C.C. Powers, S.A. Stewart, R.L. Jilka, A.M. Parfitt, S.C. Manolagas, The skeletal
810 effects of glucocorticoid excess override those of orchidectomy in mice, Endocrinology 145(4) (2004) 1980-7.
- 811 [33] A. Karunaratne, L. Xi, L. Bentley, D. Sykes, A. Boyde, C.T. Esapa, N.J. Terrill, S.D.M. Brown, R.D. Cox, R.V.
812 Thakker, H.S. Gupta, Multiscale alterations in bone matrix quality increased fragility in steroid induced
813 osteoporosis, Bone 84 (2016) 15-24.
- 814 [34] S.L. Greenspan, A. Wyman, F.H. Hooven, S. Adami, S. Gehlbach, F.A. Anderson Jr, S. Boone, A.Z. Lacroix,
815 R. Lindsay, J. Coen Netelenbos, Predictors of treatment with osteoporosis medications after recent fragility
816 fractures in a multinational cohort of postmenopausal women, Journal of the American Geriatrics Society
817 60(3) (2012) 455-461.
- 818 [35] V. Elliot-Gibson, E. Bogoch, S. Jamal, D. Beaton, Practice patterns in the diagnosis and treatment of
819 osteoporosis after a fragility fracture: a systematic review, Osteoporosis Int 15(10) (2004) 767-778.
- 820 [36] H. Gupta, S. Krauss, M. Kerschnitzki, A. Karunaratne, J. Dunlop, A. Barber, P. Boesecke, S. Funari, P. Fratzl,
821 Intrafibrillar plasticity through mineral/collagen sliding is the dominant mechanism for the extreme
822 toughness of antler bone, Journal of the Mechanical Behavior of Biomedical Materials 28 (2013) 366-382.
- 823 [37] H.S. Gupta, J. Seto, W. Wagermaier, P. Zaslansky, P. Boesecke, P. Fratzl, Cooperative deformation of
824 mineral and collagen in bone at the nanoscale, Proceedings of the National Academy of Sciences of the
825 United States of America 103(47) (2006) 17741-6.
- 826 [38] E.A. Zimmermann, B. Gludovatz, E. Schaible, B. Busse, R.O. Ritchie, Fracture resistance of human cortical
827 bone across multiple length-scales at physiological strain rates, Biomaterials 35(21) (2014) 5472-5481.
- 828 [39] L. Bentley, C.T. Esapa, M.A. Nesbit, R.A. Head, H. Evans, D. Lath, C.L. Scudamore, T.A. Hough, C. Podrini,
829 F.M. Hannan, W.D. Fraser, P.I. Croucher, M.A. Brown, S.D.M. Brown, R.D. Cox, R.V. Thakker, An N-ethyl-n-
830 nitrosourea induced corticotropin-releasing hormone promoter mutation provides a mouse model for
831 endogenous glucocorticoid excess, Endocrinology 155(3) (2014) 908-922.
- 832 [40] M. Toth, A. Grossman, Glucocorticoid-induced osteoporosis: lessons from Cushing's syndrome, Clin
833 Endocrinol 79(1) (2013) 1-11.

- 834 [41] I. Jager, P. Fratzl, Mineralized collagen fibrils: A mechanical model with a staggered arrangement of
835 mineral particles, *Biophysical Journal* 79(4) (2000) 1737-1746.
- 836 [42] A. Karunaratne, C.R. Esapa, J. Hiller, A. Boyde, R. Head, J.H. Bassett, N.J. Terrill, G.R. Williams, M.A.
837 Brown, P.I. Croucher, S.D. Brown, R.D. Cox, A.H. Barber, R.V. Thakker, H.S. Gupta, Significant deterioration in
838 nanomechanical quality occurs through incomplete extrafibrillar mineralization in rachitic bone: evidence
839 from in-situ synchrotron X-ray scattering and backscattered electron imaging, *J Bone Miner Res* 27(4) (2012)
840 876-90.
- 841 [43] A. Karunaratne, A. Boyde, C.T. Esapa, J. Hiller, N.J. Terrill, S.D. Brown, R.D. Cox, R.V. Thakker, H.S. Gupta,
842 Symmetrically reduced stiffness and increased extensibility in compression and tension at the mineralized
843 fibrillar level in rachitic bone, *Bone* (2012).
- 844 [44] H.D. Barth, M.E. Launey, A.A. Macdowell, J.W. Ager, 3rd, R.O. Ritchie, On the effect of X-ray irradiation
845 on the deformation and fracture behavior of human cortical bone, *Bone* 46(6) (2010) 1475-85.
- 846 [45] H.S. Gupta, J. Seto, W. Wagermaier, P. Zaslansky, P. Boesecke, P. Fratzl, Cooperative deformation of
847 mineral and collagen in bone at the nanoscale, *Proceedings of the National Academy of Sciences of the*
848 *United States of America* 103(47) (2006) 17741-6.
- 849 [46] H.S. Gupta, W. Wagermaier, G.a. Zickler, D. Raz-Ben Aroush, S.S. Funari, P. Roschger, H.D. Wagner, P.
850 Fratzl, Nanoscale deformation mechanisms in bone, *Nano Letters* 5(10) (2005) 2108-11.
- 851 [47] W.J. Landis, K.J. Hodgens, J. Arena, M.J. Song, B.F. McEwen, Structural relations between collagen and
852 mineral in bone as determined by high voltage electron microscopic tomography, *Microscopy research and*
853 *technique* 33(2) (1996) 192-202.
- 854 [48] M. Basham, J. Filik, M.T. Wharmby, P.C. Chang, B. El Kassaby, M. Gerring, J. Aishima, K. Levik, B.C.
855 Pulford, I. Sikharulidze, Data Analysis WorkbeNch (DAWN), *Journal of Synchrotron Radiation* 22(3) (2015)
856 853-858.
- 857 [49] A. Karunaratne, C.R. Esapa, J. Hiller, A. Boyde, R. Head, J.H. Bassett, N.J. Terrill, G.R. Williams, M.A.
858 Brown, P.I. Croucher, S.D. Brown, R.D. Cox, A.H. Barber, R.V. Thakker, H.S. Gupta, Significant deterioration in
859 nanomechanical quality occurs through incomplete extrafibrillar mineralization in rachitic bone: evidence
860 from in-situ synchrotron X-ray scattering and backscattered electron imaging, *Journal of bone and mineral*
861 *research : the official journal of the American Society for Bone and Mineral Research* 27(4) (2012) 876-90.
- 862 [50] M.J. Berger, J.H. Hubbell, S.M. Seltzer, J. Chang, J.S. Coursey, R. Sukumar, D.S. Zucker, K. Olsen, XCOM:
863 Photon Cross Section Database, 2010.
- 864 [51] I. Zizak, P. Roschger, O. Paris, B.M. Misof, A. Berzlanovich, S. Bernstorff, H. Amenitsch, K. Klaushofer, P.
865 Fratzl, Characteristics of mineral particles in the human bone/cartilage interface, *J Struct Biol* 141(3) (2003)
866 208-17.
- 867 [52] H.S. Gupta, S. Schratte, W. Tesch, P. Roschger, A. Berzlanovich, T. Schoeberl, K. Klaushofer, P. Fratzl,
868 Two different correlations between nanoindentation modulus and mineral content in the bone-cartilage
869 interface, *J Struct Biol* 149(2) (2005) 138-48.
- 870 [53] D. Planchard, SOLIDWORKS 2017 Reference Guide, SDC Publications2017.
- 871 [54] Hibbett, Karlsson, Sorensen, ABAQUS/standard: User's Manual, Hibbett, Karlsson & Sorensen1998.
- 872 [55] H.J. Gao, B.H. Ji, I.L. Jager, E. Arzt, P. Fratzl, Materials become insensitive to flaws at nanoscale: Lessons
873 from nature, *Proceedings of the National Academy of Sciences of the United States of America* 100(10) (2003)
874 5597-5600.
- 875 [56] B. Ji, H. Gao, Elastic properties of nanocomposite structure of bone, *Composites Science and Technology*
876 66(9) (2006) 1209-1215.
- 877 [57] B. Bar-On, H.D. Wagner, Mechanical model for staggered bio-structure, *Journal of the Mechanics and*
878 *Physics of Solids* 59(9) (2011) 1685-1701.
- 879 [58] T.K. Hight, J.F. Brandeau, Mathematical-Modeling of the Stress-Strain Strain Rate Behavior of Bone
880 Using the Ramberg-Osgood Equation, *Journal of Biomechanics* 16(6) (1983) 445-450.
- 881 [59] W. Yang, V.R. Sherman, B. Gludovatz, E. Schaible, P. Stewart, R.O. Ritchie, M.A. Meyers, On the tear
882 resistance of skin, *Nature Communications* 6 (2015) 6649.
- 883 [60] W.H. Press, S.A. Teukolsky, W.T. Vetterling, B.P. Flannery, Numerical recipes 3rd edition: The art of
884 scientific computing, Cambridge university press2007.

885 [61] A. Vercher, E. Giner, C. Arango, J.E. Tarancón, F.J. Fuenmayor, Homogenized stiffness matrices for
886 mineralized collagen fibrils and lamellar bone using unit cell finite element models, *Biomechanics and*
887 *Modelling in Mechanobiology* 13(2) (2014) 437-449.

888 [62] A. Ural, P. Zioupos, D. Buchanan, D. Vashishth, The effect of strain rate on fracture toughness of human
889 cortical bone: A finite element study, *Journal of the Mechanical Behavior of Biomedical Materials* 4(7) (2011)
890 1021-1032.

891 [63] S. Charoenphan, A. Polchai, Finite element modeling for strain rate dependency of fracture resistance in
892 compact bone, *J Biomech Eng* 129(1) (2007) 20-5.

893 [64] U. Hansen, P. Zioupos, R. Simpson, J.D. Currey, D. Hynd, The effect of strain rate on the mechanical
894 properties of human cortical bone, *Journal of biomechanical engineering* 130(1) (2008) 011011.

895 [65] Z. Asgharpour, P. Zioupos, M. Graw, S. Peldschus, Development of a strain rate dependent material
896 model of human cortical bone for computer-aided reconstruction of injury mechanisms, *Forensic Sci Int* 236
897 (2014) 109-16.

898 [66] T.P.M. Johnson, S. Socrate, M.C. Boyce, A viscoelastic, viscoplastic model of cortical bone valid at low
899 and high strain rates, *Acta Biomater* 6(10) (2010) 4073-4080.

900 [67] A.C. Deymier-Black, F. Yuan, A. Singhal, J.D. Almer, L.C. Brinson, D.C. Dunand, Evolution of load transfer
901 between hydroxyapatite and collagen during creep deformation of bone, *Acta Biomater* 8(1) (2012) 253-61.

902 [68] J. Akbarzadeh, S. Puchegger, A. Stojanovic, H.O.K. Kirchner, W.H. Binder, S. Bernstorff, P. Zioupos, H.
903 Peterlik, Timescales of self-healing in human bone tissue and polymeric ionic liquids, *Bioinspired, Biomimetic*
904 *and Nanobiomaterials* 3(3) (2014) 123-130.

905 [69] D. Lau, O. Büyükoztürk, M.J. Buehler, Multiscale modeling of organic-inorganic interface: From
906 molecular dynamics simulation to finite element modeling, *Materials Research Society Symposium*
907 *Proceedings*, 2012, pp. 44-49.

908 [70] J.P.R.O. Orgel, T.C. Irving, A. Miller, T.J. Wess, Microfibrillar structure of type I collagen in situ,
909 *Proceedings of the National Academy of Sciences* 103(24) (2006) 9001.

910 [71] M. Liebi, M. Georgiadis, A. Menzel, P. Schneider, J. Kohlbrecher, O. Bunk, M. Guizar-Sicairos,
911 Nanostructure surveys of macroscopic specimens by small-angle scattering tensor tomography, *Nature*
912 527(7578) (2015) 349-+.

913 [72] M. Qwamizadeh, Z. Zhang, K. Zhou, Y.W. Zhang, On the relationship between the dynamic behavior and
914 nanoscale staggered structure of the bone, *Journal of the Mechanics and Physics of Solids* 78 (2015) 17-31.

915 [73] M.-M. Giraud-Guille, Plywood structures in nature, *Current Opinion in Solid State and Materials Science*
916 3(3) (1998) 221-227.

917 [74] M.J. Turunen, J.D. Kaspersen, U. Olsson, M. Guizar-Sicairos, M. Bech, F. Schaff, M. Tägil, J.S. Jurvelin, H.
918 Isaksson, Bone mineral crystal size and organization vary across mature rat bone cortex, *Journal of Structural*
919 *Biology* 195(3) (2016) 337-344.

920 [75] A.A. Poundarik, T. Diab, G.E. Sroga, A. Ural, A.L. Boskey, C.M. Gungberg, D. Vashishth, Dilatational band
921 formation in bone, *Proceedings of the National Academy of Sciences of the United States of America* 109(47)
922 (2012) 19178-83.

923 [76] T. Hassenkam, G.E. Fantner, J.A. Cutroni, J.C. Weaver, D.E. Morse, P.K. Hansma, High-resolution AFM
924 imaging of intact and fractured trabecular bone, *Bone* 35(1) (2004) 4-10.

925 [77] Y. Wang, S. Von Euw, G. Laurent, C. Crevant, L. Bonhomme-Coury, M.M. Giraud-Guille, F. Babonneau, N.
926 Nassif, T. Azais, Impact of collagen confinement vs. ionic substitutions on the local disorder in bone and
927 biomimetic apatites, *Mater Horizons* 1(2) (2014) 224-231.

928 [78] W.Y. Ching, P. Rulis, A. Misra, Ab initio elastic properties and tensile strength of crystalline
929 hydroxyapatite, *Acta Biomater* 5(8) (2009) 3067-3075.

930 [79] Y. Bouligand, Twisted fibrous arrangements in biological materials and cholesteric mesophases, *Tissue*
931 *and Cell* 4(2) (1972) 189-217.

Table

	Strain rate (s ⁻¹)	Wild-type	GIOP	P-value
Effective fibril moduli (GPa)	0.004	13.60 ± 3.00	14.46 ± 2.66	0.876
	0.01	37.90 ± 9.90	13.02 ± 4.28	< 0.001
	0.02	65.60 ± 11.40	11.50 ± 3.58	< 0.001
Effective mineral moduli (GPa)	0.004	44.20 ± 7.29	17.90 ± 5.30	0.032
	0.01	70.50 ± 16.70	20.77 ± 1.42	< 0.001
	0.02	97.49 ± 28.38	26.66 ± 10.50	< 0.001
Reorientation rate (degree / %)	0.004	40.75 ± 23.22	2.18 ± 9.65	< 0.001
	0.01	4.90 ± 3.91	1.76 ± 5.63	0.703
	0.02	5.50 ± 4.94	1.24 ± 4.02	0.606

Figure 1

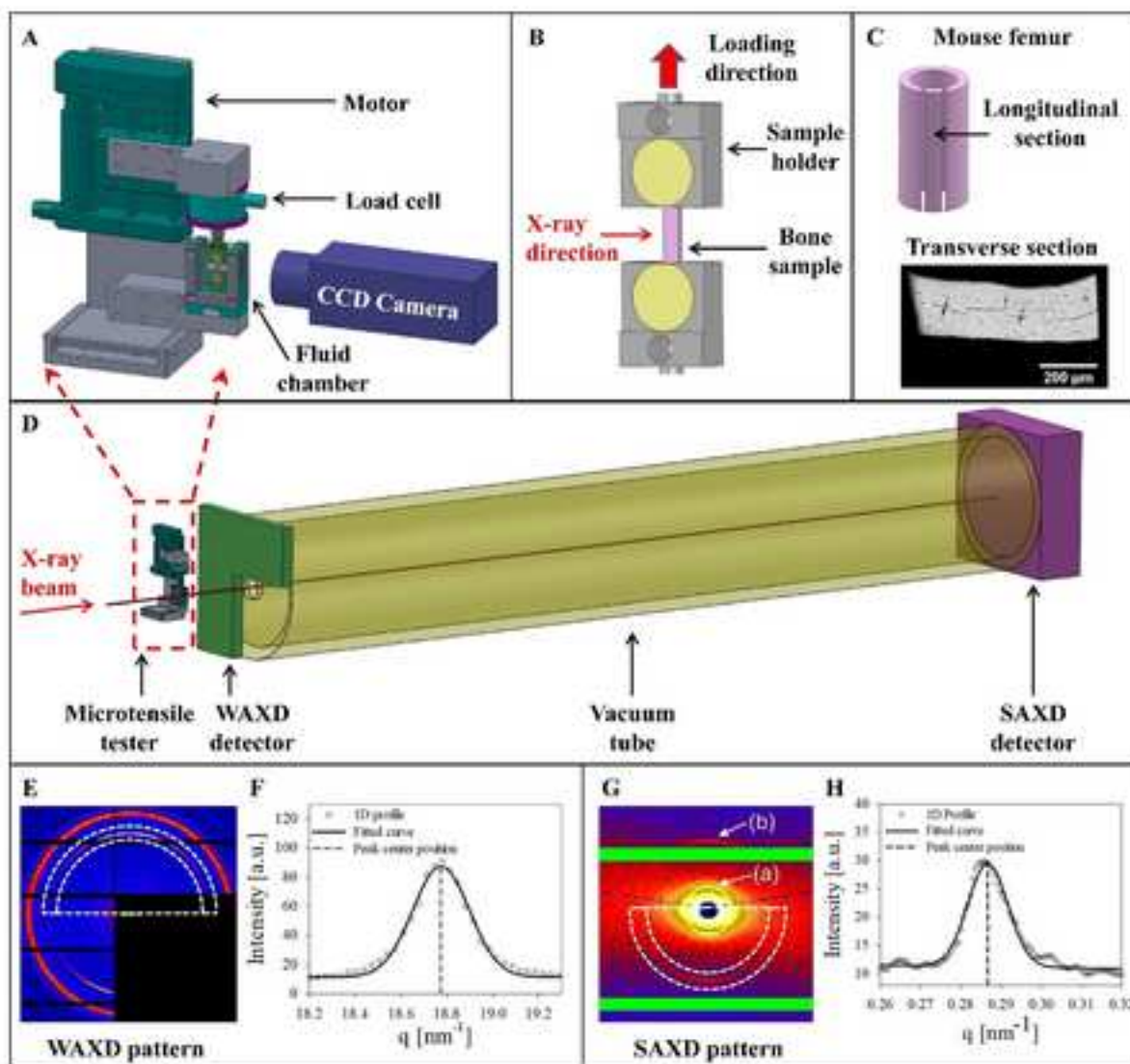


Figure 2

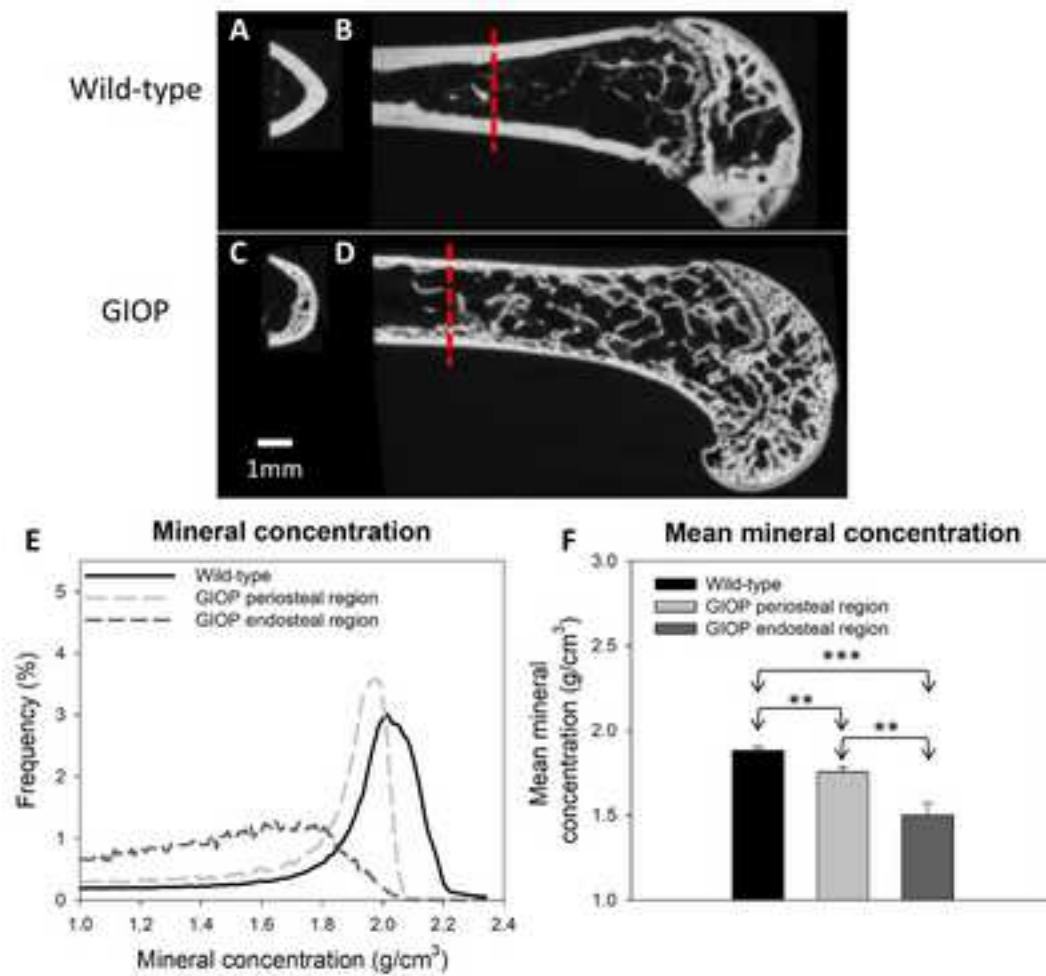


Figure 3

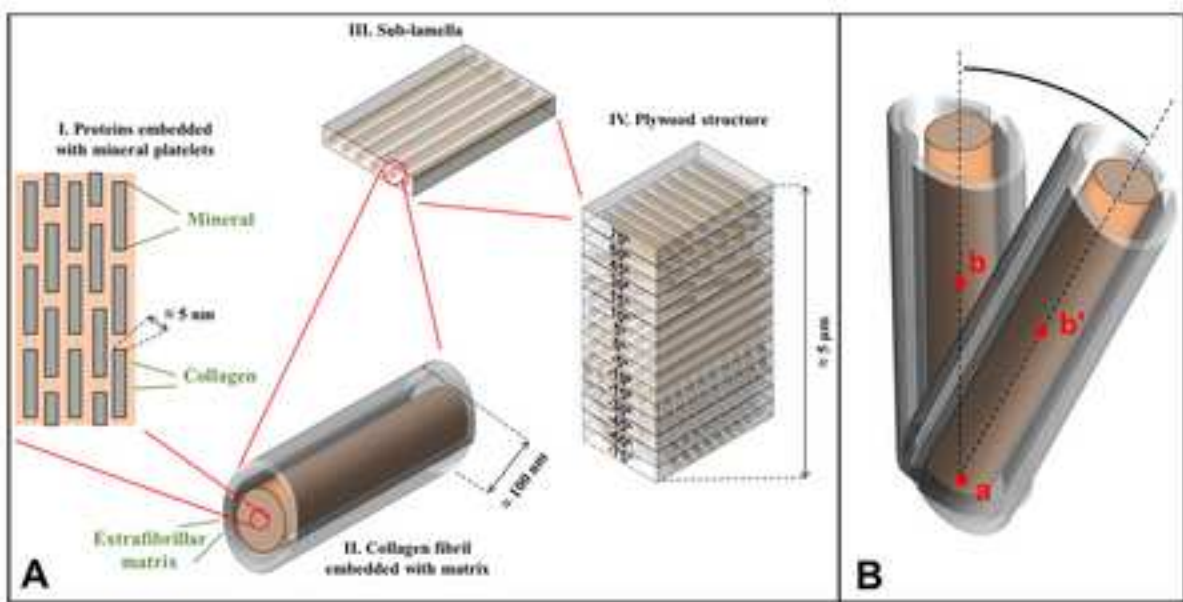


Figure 4

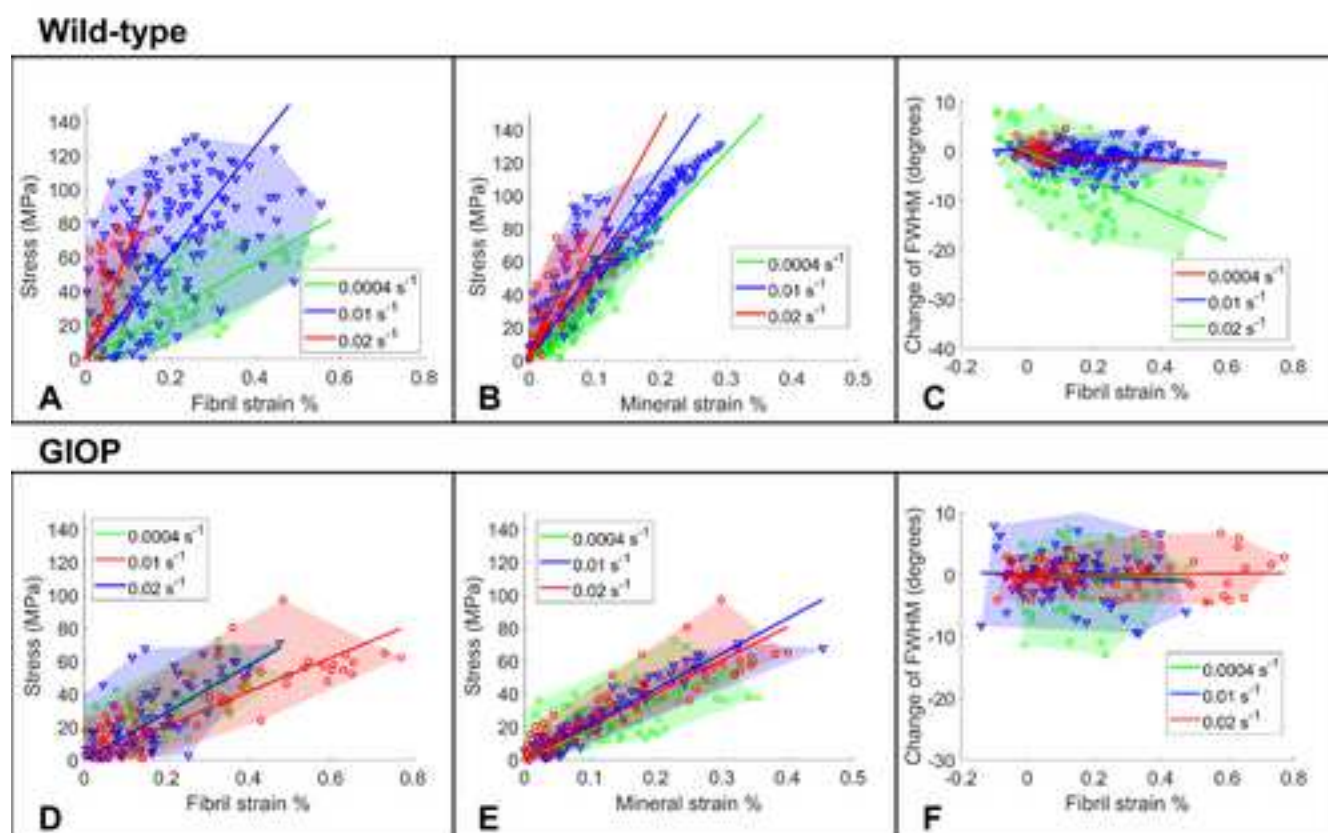
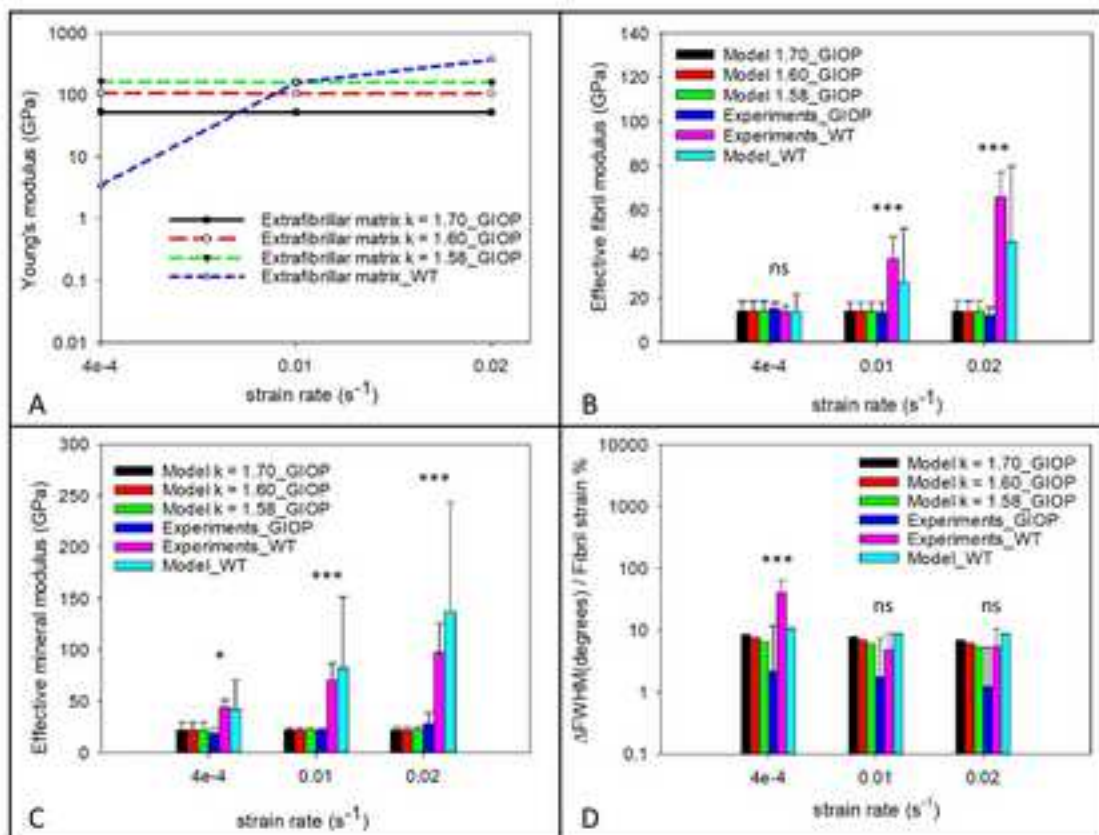


Figure 5



Supplementary Material

[Click here to download Supplementary Material: Li_strain rate_GIOP_FINAL_RFINAL_SI.docx](#)